J. Fluid Mech. (2009), *vol.* 640, *pp.* 265–303.
doi:10.1017/S0022112009991340

Axisymmetric dynamics of a bubble near a plane wall

C. W. M. VAN DER GELD† AND J. G. M. KUERTEN

Department of Mechanical Engineering, Thermo Fluids Engineering Division, Eindhoven University of Technology, P.O. Box 513, 5600 MB Eindhoven, The Netherlands

(Received 15 May 2008; revised 23 July 2009; accepted 23 July 2009; first published online 2 November 2009)

Explicit expressions for the added mass tensor of a bubble in strongly nonlinear deformation and motion near a plane wall are presented. Time evolutions and interconnections of added mass components are derived analytically and analysed. Interface dynamics have been predicted with two methods, assuming that the flow is irrotational, that the fluid is perfect and with the neglect of gravity. The assumptions that gravity and viscosity are negligible are verified by investigating their effects and by quantifying their impact in some cases of strong deformation, and criteria are presented to specify the conditions of their validity. The two methods are an analytical one and the boundary element method, and good agreement is found. It is explained why a strongly deforming bubble is decelerated. The classical Rayleigh–Plesset equation is extended with terms to account for arbitrary, axisymmetric deformation and to account for the proximity of a wall. An expression for the corresponding cycle frequency that is valid in the vicinity of the wall is derived. An equation similar to the Rayleigh–Plesset equation is presented for the most important anisotropic deformation mode. Well-known expressions for the angular frequencies of some periodic solutions without a wall follow easily from the equations presented. A periodically deforming bubble without initial velocity of the centroid and without a dominating isotropic deformation component is eventually always driven towards the wall. A simplified equation of motion of the centre of a deforming bubble is presented. If desired, full deformation computations can be speeded up by selecting an artificially low value of the polytropic constant C_p/C_v.

1. Introduction

Many submerged bodies or structures in ocean engineering and in process equipment can be deforming strongly either near a similar body or near a wall. In some of these situations the hypothesis of an ideal fluid (inviscid and irrotational) can be used. If the deformation of a solid body is unaffected by gravity and if viscous effects are negligible, the analysis of the present paper is applicable. The assumptions that gravity and viscosity are negligible will be verified by theoretically investigating their effects, by quantifying their impact in some cases of strong deformation and by quantifying criteria for their validity. A boiling bubble, as another example, grows typically from a radius of 0 to one of 0.5 mm in 1 ms. Even with forced convection, practically no wake occurs and vorticity generated at the bubble–fluid interface is confined to a thin layer at this surface. After detachment from the wall into a

† Email address for correspondence: c.w.m.v.d.geld@tue.nl

liquid at saturation temperature, the bubble wake is still undeveloped for some time, while the bubble is moving and may be experiencing strong deformation. In this isothermal situation thermocapillary stresses, the so-called Marangoni effect, do not affect interface motion and heat transfer and phase change can be ignored. If the velocity field that approaches the bubble is uniform, the ideal fluid hypothesis is applicable. For oscillatory deformation, viscous damping will be seen to be negligible if the initial bubble radius exceeds a certain threshold. It will be investigated whether and to what extent shape deformations affect motion of the bubble away from the wall. The rate at which vapour bubbles are transported to the centre of a pipe affects the net heat transfer rate from the wall in nucleate flow boiling. In particular, at conditions which are favourable for the generation of large vapour bubbles, that is, at low system pressure and/or in microgravity, shape deformation and oscillation may become important. Criteria will be given to indicate the conditions of validity of the neglect of gravity and viscous effects in the analysis.

The dynamics of a *non-deforming* bubble is given by a six-dimensional set of differential equations (Kirchhoff equations), as explained by Lamb (1932). The motion of a spherical non-deforming bubble near a plane wall is governed by the dependencies of the added mass components on a single geometrical parameter, which is the ratio of distance to the wall to sphere diameter (Lamb 1932). When the bubble is isotropically deforming, that is, a shrinking or an expanding sphere, other dependencies of the added mass tensor are involved (Geld 2002). The more complex the deformation, the more added mass coefficients and the more dependencies come into play. It will be shown that a clear separation exists in the dependencies of the added mass coefficients on shape deformation and on wall interaction. Only one parameter out of those that determine the added mass coefficients accounts for the presence of the wall, all the other parameters account for deformation.

There are good reasons to believe that the added mass tensor derived by inviscid theory is also applicable to vorticity carrying flow. Several important contributions towards an improved understanding of the added mass force have been made in the past decade (Auton, Hunt & Prud'Homme 1988; Pelekasis & Tsamopoulos 1993; Howe 1995; Magnaudet & Eames 2000; Mougin & Magnaudet 2002; Bagchi & Balachandar 2003). Most of them deal with temporal accelerations of the relative motion of fluid and a non-deformable body. The concept of added mass turns out to be well defined also at moderate Reynolds numbers. Rigorous proof that the added mass coefficients do not depend on the presence of vorticity exists for the case of constant bubble volume (Howe 1995) and for some deformation cases (Legendre, Borée & Magnaudet 1998) (see also the review by Geld 2009). Motivated by these findings, and by the applications mentioned above, this paper is dedicated to a study of the dynamics and the added mass tensor of a bubble that experiences strong deformation and is moving near a plane wall in an ideal fluid. Interaction of translational motion and deformation is highlighted.

The problem of a gas or vapour bubble moving suddenly away from a plane wall and experiencing strong shape oscillations that affect its motion is a classical hydrodynamic problem of impulsive motion that is essentially nonlinear. The nonlinearity is introduced through the impermeable body and wall boundary conditions. Benjamin & Ellis (1990) derived an expression for the drift velocity of an oscillating bubble in the absence of a wall. When the dynamics of surface deformation modes is known, it is possible to compute the drift velocity that results from second-order interactions between surface deformation modes. Mei & Zhou (1991) studied nonlinear resonance between two neighbouring shape modes and volume oscillations. They neglected

coupling of the translational motion of the bubble with the dynamics of the shape modes. Meiron (1989) computed the ellipsoidal shape of a bubble in steady rectilinear motion in an infinite fluid. He assumed the pressure in the bubble to be constant and did not study dynamics at all. Other authors (Longuet-Higgins 1989*a*,*b*,*c*; Tsamopoulos & Brown 1983) performed a perturbation analysis to derive nonlinear corrections of shape deformation of a bubble in an infinite liquid. Their findings will be compared with results of the present study. Feng & Leal (1995) derived coupled equations for the dynamics of the bubble centroid, volume oscillations and two adjacent shape modes. The main application is an acoustically driven bubble in the absence of a wall. Doinikov (2004) performed a similar analysis, but allowed for all shape modes while removing limitations on natural frequencies. In both studies a perturbation analysis was applied where the amplitudes of the shape modes and the translational velocity of the bubble are small with respect to the initial radius and to the time rate of change of the radius, respectively.

In the present study these limitations are discarded while the translational motion of the centroid occurs in the vicinity of a plane wall. It is assumed that at all times the bubble is star-shaped and axisymmetric, that is, can be described by a single function of the longitudinal angle. Expressions for all components of the added mass tensor are derived, and with the aid of the Euler–Lagrange formalism the coupled governing equations are derived and an analytical solution obtained. The effect of the wall on dynamics and added mass tensor of an initially spherical bubble is studied for two generic cases:

(i) impulsive start of deformation of arbitrary shape mode, and

(ii) impulsive start of motion perpendicular to the wall.

It will be investigated whether the first initial condition, strong deformation close to a wall, is sufficient to move bubbles away from the wall. Time histories of added mass tensor coefficients are analysed, and the main agencies affecting the motion of the centroid and affecting deformation are determined. For comparison, the resulting bubble deformation and motion are alternatively computed with the boundary element method (BEM). Further validation is obtained from comparison of added mass tensor histories with analytical solutions of special cases, one such case being given by results of a previous study (Geld 2002). In the latter study, added mass coefficients for isotropic deformation were defined, whereas in the present study many added mass coefficients are needed to account for more general shape deformation.

A new form of the well-known Rayleigh–Plesset equation is presented with terms to account for shape deformation and the proximity of a plane wall. An equation that governs anisotropic shape deformation, similar to the Rayleigh–Plesset equation, is derived. Alternative derivations for the angular frequencies of periodic solutions are presented. Frequency doubling of the fundamental radian oscillation mode will be explained. The resonance case introduced by Longuet-Hggins (1989*a*) will be analysed.

To facilitate reduction of the number of added mass coefficients required for computational fluid dynamics (CFD) computations of interactions between multiple bubbles and a wall it will be investigated which coefficients are dominant in some typical cases. A simplification of the governing equations is sought that would not essentially affect predictions of a complex system of deforming bubbles near a wall.

The problem definition is given in § 2.1. The analytical method is described in § 2.2, and the BEM in § 2.3. Results for impulsive start of deformation near a plane wall are described in § 3.5, and those for impulsive start from rest in § 3.6. Main conclusions are summarized in § 4.

2. Methods

2.1. *Problem statement*

A deforming bubble moves near a plane solid boundary in an incompressible fluid. Fluid motion is irrotational. Only cases will be considered in which purely radial oscillations are unforced and viscous damping is negligible. According to Lamb (1932, p. 641) and Longuet-Higgins (1989*b*, p. 552), this implies that the initial bubble radius $R_{t=0}$ is taken to satisfy

$$(R_{t=0}(k-2)k(k+1))^{1/4} \gg (4\nu^2\rho_L/\sigma)^{1/4}$$

for any integer k exceeding 2. Here ν denotes the kinematic viscosity of the liquid and σ the surface tension coefficient. Longuet-Higgins (1989*b*) made a small mistake leading to an overestimate of the minimum bubble radius required. For water at normal conditions it suffices that the bubble radius exceeds 0.02 mm. That this is an excessively small value was already remarked for globes of liquid by Lamb (1932). Note that the potential flow solution of an expanding sphere satisfies the full Navier–Stokes equations. Thermal and radiation losses are negligible if viscous damping is (Eller 1970; Prosperetti 1977). This will be quantified in § 3.5.5.

The bubble is star-shaped. For sake of brevity and clarity, axial symmetry is assumed around an axis perpendicular to the wall. Its contour $\partial\Omega$, the bubble liquid–vapour interface, is described by a single planar C^∞ curve. The bubble is initially spherical with radius $R_{t=0}$. Initially, at each point at the bubble interface either the velocity (analytical approach of § 2.2) or the velocity potential (BEM approach of § 2.3) is given. It is assumed that the bubble behaves polytropically, so that the pressure inside the bubble p_B and the bubble volume $\mathcal{V}$ are related by $p_B\mathcal{V}^\gamma = c$, a constant. Here γ is a constant for isentropic processes given by C_p/C_v, the ratio of the specific heats. The initial bubble pressure $p_{B,0}$ exceeds the homogeneous liquid pressure by $2\sigma/R_{t=0}$. If bubble dynamics are slow relative to the processes of heat and mass transfer, the bubble interior may be assumed to remain isothermal ($\gamma = 1$). If bubble motion is rapid, heat and vapour have insufficient time to diffuse across the bubble interior. The thermal process is effectively adiabatic in that case ($\gamma = 1.4$).

2.2. *Analytical approach*

In this section the analytical approach for modelling three-dimensional axisymmetric bubble deformation in a potential flow field is presented. It is based on the Euler–Lagrange method that employs generalized coordinates that are now defined.

Consider a bubble that occupies a region Ω with boundary $\partial\Omega$. A mirror bubble is used to simulate a plane solid wall. Let the function $R(\theta, t)$ describe the bubble interface. Here θ denotes the polar angle in a spherical coordinate system (r, θ, ψ) such that $\theta = 0$ for the point nearest to a plane infinite solid wall (see figure 1). Function R is expanded in a series of Legendre polynomials P_{n-1}. Indices i, j, l, m, n, p, q denote non-zero positive integers. Index k is reserved for § 3.5. The second term $b_2 P_1$ of the expansion

$$R(\theta, t) = \sum_{m=1}^{\infty} b_m(t)\, P_{m-1}(\cos\theta) \tag{2.1}$$

corresponds to translation of the bubble as a whole. It is always possible to select the origin of the coordinate system $\boldsymbol{x}_{orig}$ such that b_2 is zero. Select the origin for which $b_2 = 0$, and let $z/2$ be the distance of $\boldsymbol{x}_{orig}$ from the wall. Because of axial symmetry it suffices to take $z/2$ as a generalized coordinate to specify $\boldsymbol{x}_{orig}$. Velocity U, positive if away from the wall, is the corresponding generalized velocity. Parameter

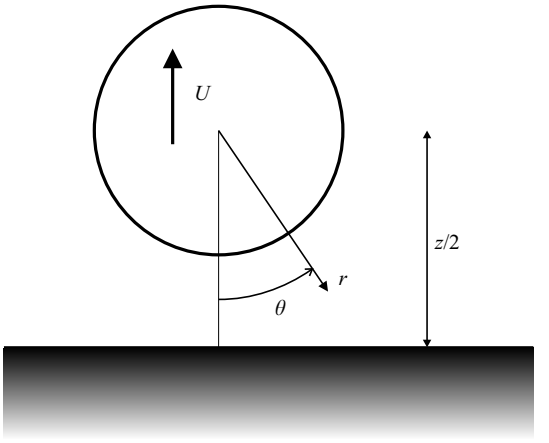

FIGURE 1. Schematic of bubble at distance $z/2$ from a plane wall, with polar angle θ and velocity U that is positive if away from the wall.

b_2 is obviously redundant and cannot be used as a generalized coordinate. All other coefficients b_m are generalized coordinates since they are independent and required to describe arbitrary deformation. Also the corresponding agencies delivering work are independent from one another, which will be employed in the derivation of expressions for the generalized forces below (defined in (2.17)).

The plane wall is modelled with the aid of a mirror bubble. Because of mirror symmetry, only a single set of coefficients $\{a_m\}$ is needed to specify the velocity potential ϕ that satisfies the Laplace equation $\Delta\phi = 0$:

$$\phi = \sum_{m=1}^{\infty} P_{m-1} \left[a_m(t)\, r^{-m} + \sum_{q=1}^{\infty} \Gamma_{mq}\; a_q(t)\, r^{m-1} \right] \tag{2.2}$$

with $\{\Gamma_{mq}\}$ a set of coefficients that account for the presence of the wall and that depend on a single generalized coordinate (see Hobson 1955):

$$\Gamma_{mq} \overset{\text{def}}{=} \binom{q+m-2}{m-1} z^{-m-q+1}.$$

At a given instant of time, the generalized coordinates,

$$(q_1, q_2, q_3, q_4, \ldots) = (b_1, z/2, b_3, b_4, \ldots),$$

as well as their corresponding generalized velocities,

$$(\dot{q}_1, \dot{q}_2, \dot{q}_3, \ldots) = (\dot{b}_1, U, \dot{b}_3, \dot{b}_4, \ldots),$$

are supposedly known or can be computed from specific velocities at $\partial\Omega$. Here, the dot denotes derivative with respect to time. It will now be shown how the time-dependent coefficients of the velocity potential $\{a_m\}$ can be determined. Thereafter, the generalized forces will be specified and Euler–Lagrange equations used to find a closed solution for the unknowns

$$(\ddot{q}_1, \ddot{q}_2, \ddot{q}_3, \ddot{q}_4, \ldots) = (\ddot{b}_1, \dot{U}, \ddot{b}_3, \ddot{b}_4, \ldots).$$

The kinematic boundary condition expresses the fact that the normal component of the velocity at a point of the bubble interface, $\boldsymbol{x}_c = (R(\theta, t), \theta)$, equals the normal

component of the liquid velocity $\boldsymbol{u}$ there:

$$\boldsymbol{n} \cdot \frac{\mathrm{d}\boldsymbol{x}_c}{\mathrm{d}t} = \boldsymbol{n} \cdot \boldsymbol{u}(\boldsymbol{x}_c, t), \tag{2.3}$$

with $\boldsymbol{n}$ the unit normal on $\partial\Omega$ that points into the fluid region. Since powers of R occur in $\boldsymbol{n} \cdot \boldsymbol{u} = \boldsymbol{n} \cdot \nabla\phi|_{r=R}$ (see (2.2)), it is convenient to define coefficients e_{nml} and d_{ij} in the following way. The constants $\{e_{nml}\}$ in the defining equation

$$P_{n-1}\, P_{m-1} = \sum_{l=1} e_{nml}\, P_{l-1} \tag{2.4}$$

are structural coefficients, that is, constants that do not depend on time or other parameters. Explicit expressions for the $\{e_{kml}\}$ are given in terms of $\eta_m \stackrel{\text{def}}{=} (2m-1)!!/m!$ by Gradsteyn & Ryzhyk (1980, § 8.915). These e_{nml}-coefficients can also be expressed in terms of Clebsch–Gordan coefficients (Abramowitz & Stegun 1972). The sum in (2.4) is finite. For i in $\mathbb{Z}$, coefficients d_{ij} are defined by

$$R^i = \sum_{j=1}^{\infty} d_{ij}\, P_{j-1}. \tag{2.5}$$

The coefficients d_{ij} depend on the b_m which depend on time.

The kinematic boundary condition (2.3) yields

$$\sum_{m=1}^{\infty} \dot{b}_m\, P_{m-1}\, R + U\, P_1^1 \sum_{n=1}^{\infty} b_n\, P_{n-1}^1 - U\, P_1\, R = R\, \left.\frac{\partial\phi}{\partial r}\right|_R - \sum_{m=1}^{\infty} b_m\, P_{m-1}^1\, R\, \left.\frac{\partial\phi}{\partial\theta}\right|_R \tag{2.6}$$

with $P_1 = \cos\theta$ and $P_1^1 = -\sin\theta$. The P_n^1 are the associated Legendre functions of the first order. Employing the summation rule (Gradsteyn & Ryzhyk 1980, § 8.915) and

$$P_n^1(\cos\theta) = \frac{1}{\sqrt{1-\cos^2\theta}}\, \frac{n\,(n+1)}{2n+1}\, \left(P_{n+1}(\cos\theta) - P_{n-1}(\cos\theta)\right), \tag{2.7}$$

it is easily shown that

$$P_{n-1}^1\, P_{j-1}^1 = -\frac{n\,(n-1)}{2n-1}\,(P_n - P_{n-2}) \sum_{l=0}^{[(j-2)/2]} (2\,j - 4\,l - 3)\, P_{j-2l-2} \tag{2.8}$$

Here $[j]$ denotes the integer part of j. The operator

$$\frac{2\,m-1}{2} \int_{-1}^{1} \mathrm{d}\,(\cos\theta)\; P_{m-1}$$

is now applied to the boundary condition (2.6). This yields

$$\sum_{n=1}^{\infty} G_{mn} a_n = \dot{b}_m + U \sum_{n=1}^{\infty} F_{mn} b_n - U\,\delta_{m2} \tag{2.9}$$

with F_{mn} and G_{mn} the following functions of the b_i-coefficients:

$$F_{mn} = \sum_i d_{(-1)i}\, \omega_{mni2} = \sum_i d_{(-1)i}\, \frac{n(n-1)}{1-2n} (e_{i(n+1)m} - e_{i(n-1)m}) \tag{2.10}$$

and

$$G_{mn} = -n\sum_i d_{(-n-1)i}\,e_{inm} - \sum_{i,q} d_{(-n-2)i}\,b_q\,\omega_{mqin} + \Gamma_{2n}\delta_{m2} + \sum_{j,i}(j+1)\Gamma_{(j+2)n}\,d_{ji}\,e_{i(j+2)m} - \Gamma_{2n}\sum_{i,q} d_{(-1)i}\,b_q\,\omega_{mqi2} - \sum_{f,i,q}\Gamma_{(f+2)n}\,d_{(f-1)i}\,b_q\,\omega_{mqi(f+2)} \tag{2.11}$$

Here the set of structural coefficients $\{\omega_{mnfj}\}$ is defined by

$$\omega_{mnfj} \overset{\text{def}}{=} \frac{2m-1}{2}\int_{-1}^{1} \mathrm{d}w\; P_{m-1}(w)P_{f-1}(w)P^1_{n-1}(w)P^1_{j-1}(w). \tag{2.12}$$

With the aid of (2.8) coefficients ω_{mnfp} can be expressed in a finite series of e_{ijp}-coefficients, as the one on the right-hand side of (2.10).

It can be shown that the set of coefficients $\{G_{mp}\}_{m,p}$ corresponds to a Hilbert–Schmidt operator $\mathbf{G}$ that possesses an inverse $\mathbf{G^{-1}}$ if one of the generalized velocities is unequal to zero. For the case $0 = b_3 = b_4 = b_5 = \ldots$, that is, the case of isotropic deformation, a proof is given by Geld (2002); a general proof is a straightforward but lengthy extension. Application of $\mathbf{G^{-1}}$ to the equivalent of (2.9), written in terms of $\mathbf{G}$, yields the coefficients a_j of the velocity potential.

The velocity potential is now used to compute the kinetic energy in the fluid domain Ω, that is, the half space without the bubble. This energy of the fluid T can be written as the following quadratic function of the generalized velocities:

$$T/\{\rho_L \cdot \mathscr{V}\} = \frac{1}{2}\alpha U^2 + \frac{1}{2}U\sum_{m=1}^{\infty}\gamma_m\dot{b}_m + \frac{1}{2}\sum_{i,j}^{\infty}\psi_{ij}\dot{b}_i\dot{b}_j, \tag{2.13}$$

where ρ_L denotes the mass density of the liquid. The coefficients α, γ_m and ψ_{ij} only depend on time and the generalized coordinates, and together constitute the added mass tensor of the bubble.

Let G^{-1}_{pm} denote the element $(G^{-1})_{pm}$ of the inverse operator $\mathbf{G}$ for arbitrary non-zero integers p and m. Straightforward computations yield

$$\begin{aligned}
\psi_{ml} &= -\frac{2}{2m-1}(2\pi/\mathscr{V})\sum_n G^{-1}_{nl}\left[\sum_j d_{(-n+2)j}\,e_{njm} + \sum_p \Gamma_{pn}\sum_j d_{(p+1)j}\,e_{pjm}\right],\\
\gamma_m &= -\psi_{m2} + \sum_{q,i,j}\psi_{mq}\,d_{(-1)i}\,b_j\,\omega_{qji2} - (2\pi/\mathscr{V})\sum_p G^{-1}_{pm}\\
&\quad\times\left[\sum_j d_{(-p+2)j}\,S_{pj} + \sum_n \Gamma_{np}\sum_j d_{(n+1)j}\,S_{nj}\right],\\
\alpha &= (2\pi/\mathscr{V})\sum_p\left[G^{-1}_{p2} - \sum_{i,n,m} G^{-1}_{pm}\,d_{(-1)i}\,\omega_{mni2}\,b_n\right]\\
&\quad\times\left[\sum_j d_{(-p+2)j}\,S_{pj} + \sum_{m,j}\Gamma_{mp}\,d_{(m+1)j}\,S_{mj}\right],
\end{aligned} \tag{2.14}$$

where ω_{mni2} can be replaced by the explicit expression given in (2.10) and S_{kj} is defined by

$$S_{nj} \stackrel{\text{def}}{=} -\frac{2}{3}\,e_{nj2} + \sum_l d_{(-1)l} \sum_{i,p} e_{nlp}\, e_{pji} \cdot \left\{ \frac{2i(i+1)}{(2i+1)(2i-1)} b_{i+1} - \frac{2(i-1)(i-2)}{(2i-3)(2i-1)} b_{i-1} \right\}. \tag{2.15}$$

To each generalized variable q_j corresponds an Euler–Lagrange equation of the form

$$\frac{\mathrm{d}}{\mathrm{d}t}\frac{\partial T}{\partial \dot{q}_j} - \frac{\partial T}{\partial q_j} = Q_j \tag{2.16}$$

with Q_j the generalized forces, in general also including conservative forces. The generalized forces are in this case given by

$$Q_j = (p_B - p_\infty)\frac{\partial \mathcal{V}}{\partial q_j} - \sigma \frac{\partial A_B}{\partial q_j}. \tag{2.17}$$

Here A_B is the surface area of the bubble and p_∞ is the pressure at infinity. Note that drag and gravity are not considered in the present study. Equation (2.17) can be derived by expressing $\mathrm{d}T/\mathrm{d}t$ in terms of integrals over $\partial\Omega$ by substituting the normal stress boundary condition in order to relate to the pressure inside the bubble, by subsequent application of the surface divergence theorem to express the result in $\mathrm{d}\mathcal{V}/\mathrm{d}t$ and $\mathrm{d}A_B/\mathrm{d}t$, and by employing the fact that the agencies delivering work and corresponding to the generalized coordinates are mutually independent (Geld 2002, 2009). Coefficients g_j and h_m are now introduced in order to facilitate the determination of A_B and its derivatives with respect to the b_n. These new coefficients depend on the b_n and describe the dependence of the radial component of the normal on the polar angle:

$$n_r = \sum_{j=1}^{\infty} g_j\, P_{j-1} \qquad \frac{1}{n_r} = \sum_{m=1}^{\infty} h_m\, P_{m-1}. \tag{2.18}$$

The area A_B is given by $4\pi \sum_n d_{2n}\, h_n/(n-1)$ and

$$\frac{\partial A_B}{\partial b_n} \Big/ (2\pi) = \frac{2}{2n-1} \sum_p e_{pmn}\, b_p (h_m + g_m) + 2 \sum_{l,m} g_l\, \omega_{1mln}\, b_m.$$

It is easily seen that $\partial \mathcal{V}/\partial b_n = 4\pi\, d_{2n}/(2n-1)$. It is now straightforward to compute the generalized forces Q_j. Since the wall is fully wetted, the generalized force corresponding to $z/2$, Q_2, is zero.

Equation (2.17) makes clear that two physical parameters control the dynamics of a deforming object if gravity and viscous effects are negligible. One of them accounts for capillary effects and often the Weber number $We \stackrel{\text{def}}{=} \rho_L R_{t=0} U_0^2/\sigma$ is used as a criterion to indicate its significance. The initial radius $R_{t=0}$ in the definition of We can be replaced by a volume-based mean radius if the initial shape is non-spherical, of course. Sample computations in this paper will all start with a spherical shape. The initial velocity U_0 in the definition of the Weber number will be replaced by another generalized velocity if $U_0 = 0$. The second physical parameter in control of the dynamics corresponds to the pressure p_∞. The initial value of the pressure in the bubble p_B is related to p_∞ via the equation of state of the content of the bubble. Consistent with the definition of the Weber number, a dimensionless pressure is defined as $p_\infty/(\rho_L U_0^2)$.

The Euler–Lagrange equations (2.16) yield a set of coupled differential equations that are linear in the unknowns $(\ddot{b}_1, \dot{U}, \ddot{b}_3, \ddot{b}_4, \ldots)$, with proportionality coefficients composed solely of constants and added mass tensor coefficients. The method of reduction (Kantorovich & Krylov 1958) is applied to solve this system. To prevent aliasing, series as those of (2.18) are truncated after $8N$ terms if the series of ϕ and R are truncated after N terms. No iterative steps are required and integration in time is the only numerical step involved. This numerical step is required to specify the values of the generalized coordinates and velocities at a next instant of time. The derivatives $(\ddot{b}_1, \dot{U}, \ddot{b}_3, \ddot{b}_4, \ldots)$ are integrated with the three-step Adams–Bashforth method after start-up with Euler's method. The new coordinates are determined with an adapted three-step Adams–Bashforth algorithm that employs both the first-order derivatives $(\dot{b}_1, U, \dot{b}_3, \dot{b}_4, \ldots)$ and the second-order derivatives $(\ddot{b}_1, \dot{U}, \ddot{b}_3, \ddot{b}_4, \ldots)$. The time step is chosen sufficiently small, so that the method is both stable and accurate.

The importance of and connections between the added mass coefficients are elucidated by introduction of a symmetric matrix $\boldsymbol{A}$. It is defined as follows: $A_{ij} = \psi_{ij} = \psi_{ji}$ if both i and j are unequal to 2, $A_{2j} = A_{j2} = \gamma_j/2$ if $j \neq 2$ and $A_{22} = \alpha$. The Euler–Lagrange equations then yield the matrix equation

$$\boldsymbol{A} \cdot \ddot{\boldsymbol{b}} = \boldsymbol{c}, \tag{2.19}$$

where $\ddot{\boldsymbol{b}}$ represents the column vector $(\ddot{b}_1, \dot{U}, \ddot{b}_3, \ddot{b}_4, \ldots)^T$ and $\boldsymbol{c}$ a column vector that comprises generalized velocities and other parameters that are known at a certain instant of time. The unknown generalized accelerations $\ddot{\boldsymbol{b}}$ are determined from (2.19), and subsequent integration in time yields the generalized velocities, and $\boldsymbol{c}$, at the next instant of time. The matrix $\boldsymbol{A}$ therefore controls the dynamics of large-amplitude bubble deformation near a wall.

2.3. *Boundary element method*

In this section the numerical method used to validate the results of the analytical approach is described. The BEM is chosen since it is very suitable for problems with a deforming interface in an unbounded fluid. The BEM is based on the following. If inside a region Ω with boundary $\partial\Omega$ the velocity potential satisfies the Laplace equation $\Delta\phi = 0$, the velocity potential in an arbitrary point $\boldsymbol{x}_0 \in \partial\Omega$ obeys

$$\phi(\boldsymbol{x}_0) = -2\int_{\partial\Omega} G(\boldsymbol{x};\boldsymbol{x}_0)\frac{\partial\phi}{\partial n}(\boldsymbol{x})\,\mathrm{d}S_x + 2\int_{\partial\Omega}\phi(\boldsymbol{x})\frac{\partial G}{\partial n}(\boldsymbol{x};\boldsymbol{x}_0)\,\mathrm{d}S_x. \tag{2.20}$$

Here $G(\boldsymbol{x};\boldsymbol{x}_0) = 1/(4\pi|\boldsymbol{x} - \boldsymbol{x}_0|)$ is Green's function of the three-dimensional Laplace equation. In case the velocity potential on the boundary is known, (2.20) is an integral equation for the unknown normal derivative of the velocity potential at the boundary.

We consider the same situation as in § 2.1 and 2.2. If the plane wall is present the integrals in (2.20) extend over both the bubble and its mirror image. Due to the axisymmetry, the integrals over the azimuthal angle can be performed analytically (Pozrikidis 1997). To this end the boundary of the bubble is represented by

$$\boldsymbol{x} = (x(s), r(s)\cos\varphi, r(s)\sin\varphi),$$

with s the arclength to represent the contour C in a polar plane. This leads to

$$\begin{aligned}\phi(x_0, r_0) = -\frac{1}{2\pi}\int_C r\frac{\partial\phi}{\partial n}(x, r)I_{10}(x_0 - x, r, r_0)\,\mathrm{d}l + \frac{1}{2\pi}\int_C r\phi(x, r)\\ \times\{[(x_0 - x)n_x - rn_r]I_{30}(x_0 - x, r, r_0) + r_0 n_r I_{31}(x_0 - x, r, r_0)\}\,\mathrm{d}l,\end{aligned} \tag{2.21}$$

where n_x and n_r are the components of $\boldsymbol{n}$ in the two directions in the polar plane. Further, I_{10}, I_{30} and I_{31} are related to elliptic functions:

$$I_{10}(x_0 - x, r, r_0) = \frac{4}{((x - x_0)^2 + (r + r_0)^2)^{1/2}} F(\tilde{k}),$$

$$I_{30}(x_0 - x, r, r_0) = \frac{4}{((x - x_0)^2 + (r + r_0)^2)^{3/2}} J_{30}(\tilde{k}),$$

$$I_{31}(x_0 - x, r, r_0) = \frac{4}{((x - x_0)^2 + (r + r_0)^2)^{3/2}} J_{31}(\tilde{k}),$$

$$\tilde{k} = \frac{4rr_0}{(x - x_0)^2 + (r + r_0)^2}, \quad J_{30}(\tilde{k}) = \frac{E(\tilde{k})}{1 - \tilde{k}^2},$$

$$J_{31}(\tilde{k}) = \frac{1}{\tilde{k}^2}\left(-2F(\tilde{k}) + \frac{2 - \tilde{k}^2}{1 - \tilde{k}^2} E(\tilde{k})\right)$$

and $F(\tilde{k})$ and $E(\tilde{k})$ are the complete elliptic integrals of the first and second kind (Gradsteyn & Ryzhyk 1980).

The numerical method starts from a given shape of the bubble and a given velocity potential at the bubble surface. The tangential velocity components follow easily from $\partial\phi/\partial s$. Next, (2.21) is used to solve for $\partial\phi/\partial n$ at the bubble surface. For this purpose, collocation points are chosen on the contour of the bubble surface to which (2.21) is applied and the shape of the contour is represented by cubic B-splines (Toose *et al.* 1996). The singularity in the second integral in (2.21) is removed by a quadratic transformation (Telles 1987) and the integrals are evaluated numerically using a high-order Gauss quadrature. The resulting system of equations is solved with a direct method.

In this way, both velocity components at the bubble surface are determined and the bubble shape and velocity potential at its surface at a next instant of time follow by integration of the kinematic and dynamic boundary conditions. The kinematic boundary condition is given by equation (2.3) where $\boldsymbol{x}_c$ is now the position of a collocation point. The dynamic boundary condition follows from Bernoulli's equation and can be written as

$$\frac{\mathrm{d}\phi}{\mathrm{d}t} = \frac{1}{2}|\nabla\phi|^2 + \frac{\sigma}{\rho_L}\mathscr{C} - \frac{p_B - p_\infty}{\rho_L} + 2\frac{\mu}{\rho_L}\frac{\partial u_n}{\partial n} + \tilde{g}x_2. \tag{2.22}$$

In this equation $\mathrm{d}/\mathrm{d}t$ is the material derivative $\partial/\partial t + \nabla\phi\cdot\nabla$, $\mathscr{C}$ is the local curvature of the surface, $\mu = \nu\rho_L$ the dynamic viscosity of the liquid and $u_n \overset{\text{def}}{=} \boldsymbol{u}\cdot\boldsymbol{n}$. The local distance to the wall is x_2 and $\tilde{g}$ denotes gravitational acceleration. The term $\partial u_n/\partial n$ is evaluated from the known velocity potential, its normal derivative and $\Delta\phi = 0$, which leads to

$$\frac{\partial u_n}{\partial n} = -\frac{\partial^2\phi}{\partial s^2} - \frac{r'}{r}\frac{\partial\phi}{\partial s} - \left(x'r'' - r'x'' - \frac{x'}{r}\right)\frac{\partial\phi}{\partial n},$$

where primes denote derivatives with respect to the parameter s.

Equation (2.22) shows that two new dimensionless parameters can be defined if gravity and viscosity are accounted for. In the same way, and with similar annotations, as the Weber number was introduced, the Bond and the Reynolds numbers are defined: $Bo \overset{\text{def}}{=} \tilde{g}R_0^2\rho_L/\sigma$ and $Re \overset{\text{def}}{=} R_0U_0\rho_L/\mu$. From these definitions it is obvious that viscous effects are negligible if Re is high and that the effect of gravity can be ignored if Bo small. Examples will be given to show what values in practice are required to justify the neglect of gravity and viscous effects.

Equations (2.3) and (2.22) are integrated in time with the standard fourth-order Runge–Kutta method, which implies that (2.21) has to be solved four times in each time step. All geometric quantities, such as the bubble volume and the local curvature, are computed with the use of the spline representation and a high-order Gauss quadrature. The time step is chosen sufficiently small, so that the method is both stable and accurate. In cases with large deformation clustering of collocation points is prevented by redistributing them after every time step in such a way that they remain approximately equidistant. For the test cases shown in §§ 3.1–3.5 this redistribution was not applied.

3. Results

In this section, added mass predictions of the analytical method are presented, as well as deformation history predictions of both the analytical and BEM methods. Four comparisons with known solutions will be made. One is oscillatory motion governed by the Rayleigh–Plesset equation (§ 3.1). Another known solution is the added mass tensor of a stationary non-deforming ellipsoid without a wall (§ 3.2). A third category of known solutions are the anisotropic shape oscillations without a wall computed by Lamb (1932, pp. 117–475) (§ 3.3). Finally, in the presence of a plane wall a validation case is offered by the more recently found solutions for spherical bubble expansion near a plane wall (Geld 2002).

After these comparisons, more complicated motion and deformation cases are analysed. Two generic cases will be considered. The first case is that of a bubble whose centre is initially at rest. Motion of the centre is induced by the deformation that is set in at time zero by prescribing non-zero deformation velocities. The second case is that of an initially spherical bubble whose centre is given a velocity away from the wall. The second case is of practical relevance in boiling (see § 1). In both generic cases, the deformation and added mass coefficients are studied. The controlling dimensionless parameter (Weber number) will be varied sufficiently to cover all interesting phenomena. In all cases considered fluid viscosity is neglected and the fluid surrounding the bubble is assumed to be perfect, as argued in § 2.1. The process that the content of the bubble experiences is taken to be a polytropic one. Computations shown in figures in this paper are for $\gamma = 1.4$.

All results presented have been validated by changing the number of collocation points (BEM) or expansion coefficients (analytical method) and by changing the time step. To analyse the number of generalized coordinates required to describe the deforming shape, the following shape error is defined:

$$E_{rr} \stackrel{\text{def}}{=} \frac{1}{R_{t=0}} \sqrt{\int_0^\pi (R - R_\infty)^2 R^2 \sin(\vartheta)\, \mathrm{d}\vartheta \Big/ \int_0^\pi R^2 \sin(\vartheta)\, \mathrm{d}\vartheta}. \tag{3.1}$$

This error is the average over the entire bubble surface of the difference between the computed radius $R(\vartheta)$ and the radius computed with a large (in principle ∞) number of coefficients, $R_\infty(\vartheta)$. Figure 2 shows the dependency of the shape error on the number of shape coefficients N at various times for a deformation test case that is fully discussed in § 3.5. From figure 2 it follows that the shape error varies roughly proportionally to N^{-6} at all times. When the error is about 0.01 % maximum at all times the number of coefficients is considered to be sufficient. The value of $|b_N|$ then usually differs five orders of magnitude with the value of $|b_3|$. The gap between the bubble and the wall merely increases between time zero and time 0.341. At times

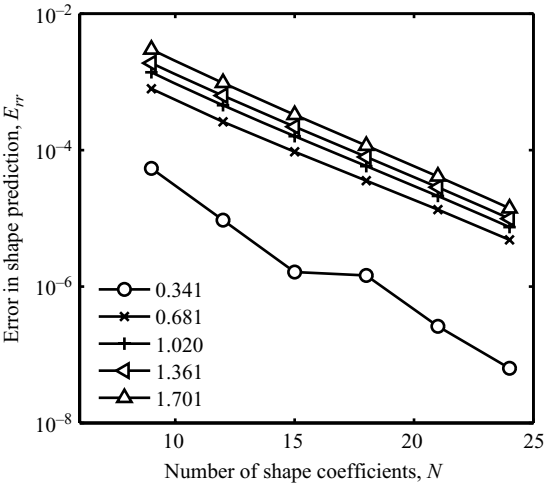

FIGURE 2. Average shape error dependence on number of shape coefficients N for various dimensionless times, $-\mathrm{d}b_3/\mathrm{d}t|_{t=0}t/R_{t=0}$, of a deformation history that will be depicted in figure 4. The error is averaged over the entire bubble surface and given relative to the initial bubble radius.

later than 0.4, this gap has got its minimal value during a cycle at least once, and the truncation error is relatively high when the gap has this minimal value. For this reason the shape errors of figure 2 are closer to each other at later times, while the error at time 0.341 is smallest. In § 3.5.2 results of the expansion method and BEM will be compared for one specific test case involving a bubble deforming close to a wall.

3.1. *No wall, isotropically deforming sphere*

The case of an expanding or shrinking spherical bubble without a wall and without motion of its centroid is the simplest case which can be calculated. The BEM computation starts with the initial velocity potential generated by a monopole at the bubble centre, that is, $\phi = \tilde{c}/|\boldsymbol{x}|$. The time evolution of the radius of the bubble is described by the Rayleigh–Plesset equation (Brennen 1995, p. 101). If the strength of the monopole $\tilde{c}$ is sufficiently small the change in radius is so small that the Rayleigh–Plesset equation can be linearized with solution

$$R(t) = R_{t=0}(1 + \beta \sin(\omega_{RP} t)),$$

where $R_{t=0}$ is the initial bubble radius and

$$\omega_{RP} = \sqrt{\frac{3\gamma p_\infty}{\rho_L R_{t=0}^2} + \frac{2(3\gamma - 1)\sigma}{\rho_L R_{t=0}^3}} \tag{3.2}$$

is the natural frequency corresponding to isotropic deformation of the bubble at pressure p_∞. A derivation of (3.2), and of modifications to account for the proximity of a wall, will be given in § 3.4 and § 3.5.7. More often than not the pressure term of (3.2) dominates the frequency ω_{RP}. A special case of ω_{RP} will be considered in § 3.5.5. Usually the time $2\pi/\omega_{RP}$ is the smallest physical time scale involved, even if deformation is anisotropic and with large amplitude, and this time determines the smallest integration time step needed in time integration, the only numerical step in the analytical method of § 2.2. Amplitude β is related to the monopole strength by

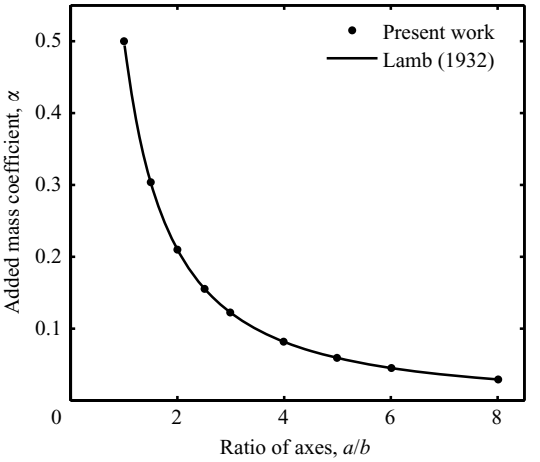

FIGURE 3. Comparison of added mass coefficients of an oblate ellipsoid given by Lamb (1932) and the analytical method of § 2.2.

$\beta = -\tilde{c}/\omega_{RP} R_{t=0}^3$. The analytical method starts with

$$\dot{b}_1\big|_{t=0} = R_{t=0}\,\beta\,\omega_{RP}$$

and a spherical shape, which yields the same monopole strength. Both the analytical results and the numerical result are in good agreement with the solution of the linearized Rayleigh–Plesset equation. For the analytical method this is no surprise since the Euler–Lagrange equation for b_1, that is, the first row-equation of (2.19), for this case reduces to the classical Rayleigh–Plesset equation. Extensions of the Rayleigh–Plesset equation will be presented in § 3.4 and § 3.5.4. Even after hundreds of oscillations no difference in phase or amplitude can be seen between the analytical and numerical solution.

3.2. *No wall, non-deforming ellipsoid*

The added mass coefficient corresponding to motion of a prolate non-deforming ellipsoid in the direction of its longest axis in an unbounded fluid α (see (2.13)) was analytically computed by Lamb (1932, p. 153). Let the longest axis have length a, and the shortest axis have length b. The numeric eccentricity e is given by $1-(b/a)^2 = e^2$. The solution of Lamb is $\alpha = \alpha_0/(2-\alpha_0)$ with

$$\alpha_0 = 2(1-e^2)e^{-3}\left\{\frac{1}{2}\ln((1+e)/(1-e)) - e\right\}.$$

This solution, as well as some values that were tabulated by Lamb, are given in figure 3. To apply the method of § 2.2, the contour of the ellipsoid, given by

$$R(\vartheta) = b/\sqrt{\{1-e^2\cos^2(\vartheta)\}},$$

is expanded in the series given by (2.1). The more the eccentricity deviates from 1, the more coefficients b_m are required to describe the contour properly, and because of reflectional symmetry $0 = b_2 = b_4 = b_6 = \ldots$. The coefficients g_j of the normal (see (2.18)) have a similar property. Values of added mass α obtained from (2.14) represented by discrete dots in figure 3 are the same as corresponding values tabulated by Lamb.

3.3. *Anisotropic, small deformation not very close to a wall*

If a gas–liquid interface is axial-symmetric, it is conveniently described by the time-dependent coefficients b_j of expansion (2.1): $R = \sum_{j=1}^{\infty} b_j P_{j-1}(\cos(\theta))$ (see § 2.2). Consider an initially spherical bubble. Let k be 3, 4, 5, ..., and let excitation of mode k, or b_k-excitation, be defined as the initial condition given by $b_1 = R_{t=0}, 0 = b_2 = b_3 = b_4 = \ldots, U = 0, \dot{b}_j = 0$ for $j \neq k$, and $\dot{b}_k \neq 0$. Counter k is taken to exceed 2 since excitation of coefficient b_1 is a special case (see § 3.1 and § 3.4) and since coefficient b_2 corresponds to motion of the interface as a whole (see § 2.2). In the absence of a wall no preferred direction of motion exists, and coefficient b_2, selected to be zero, simply disappears. In the presence of a wall, motion perpendicular to the wall can be induced. The distance of the centre of the bubble to the wall, $z/2$, is the generalized coordinate that replaces b_2, and the initial value of z, z_0, may affect excitation of mode k.

Excitation of mode k in the absence of a wall leads to an oscillatory change of this b_k-coefficient at a well-known frequency (Lamb 1932) to be derived in an alternative way below. This frequency is constant because viscous dissipation is neglected. Even in the presence of a plane wall, expressions of the analytical approach, § 2.2, permit to derive the governing frequency in the following way.

Define $\tilde{f} \overset{\text{def}}{=} b_k/b_1$, $g \overset{\text{def}}{=} b_1/z$ and write

$$R = b_1(1 + \tilde{f} P_{k-1}) = R_{t=0}(1 + \tilde{\beta}(t))\{1 + \tilde{f}(t) P_{k-1}(\cos(\vartheta))\}. \tag{3.3}$$

Before linearizing the kth row-equation of equation (2.19) it is divided by $(\partial \mathscr{V}_B/\partial b_k)/\tilde{f}$ for which the following approximation is used:

$$\frac{\partial \mathscr{V}_B}{\partial b_k} \Big/ \tilde{f} \approx \frac{8\pi}{2k-1} b_1^2. \tag{3.4}$$

Specify small deformation by requiring $\tilde{f}^2 \ll 1$ and $\tilde{\beta}^2 \ll 1$ at all times. Specify 'not very close to a wall' by requiring that terms with g and g^2 are retained while terms in g^3 and higher orders of g are negligible. More specifically, let $|g^4| = |(b_1/z)^4| \ll 1$, but let it be possible that the orders of magnitude of g^2 and $|\tilde{f}|$ are the same. Note that $|g| \leqslant 0.5$ everywhere, making the condition $|g^4| \ll 1$ satisfied at all places not in the vicinity of the wall. It can now be derived that

$$\frac{\partial A_B}{\partial b_k} R_{t=0} \Big/ \frac{\partial \mathscr{V}_B}{\partial b_k} \approx 2 + \tfrac{1}{2}(k+1)(k-2) \tag{3.5}$$

and that

$$\psi_{kk} \approx \frac{3}{k(2k-1)} \left(1 + \frac{(2k-2)!}{\{(k-1)!\}^2} g^{2k-1}\right) \approx 3/(k(2k-1)) \,. \tag{3.6}$$

Equations (3.4)–(3.6) hold also for $k = 1$ and are used to approximate terms in the linearized kth row-equation of (2.19) with $\boldsymbol{c}$ containing the right-hand side of (2.17). Since $p_\infty = p_{B,0} - 2\sigma/R_{t=0}$ and

$$p_B - p_{B,0} \approx -3\gamma \tilde{\beta} p_{B,0},$$

the linearized equation (terms in $\tilde{f}^2, g^2, fg, U$ are negligible) can be written as

$$\ddot{b}_k \approx -k(k+1)(k-2) \frac{\sigma}{\rho_L R_{t=0}^3} b_k. \tag{3.7}$$

It is noted that for any $k \geqslant 3$, the term $(2k-2)! g^{2k-1}/\{(k-1)!\}^2$ of (3.6) that is neglected in (3.7) is less than 0.06 if $g \leqslant 0.4$ (note that $g = 1/2$ corresponds to a sphere

touching the wall). With the value 0.06 the governing frequency derived from (3.7) is reduced by about 3 % due to changes in ψ_{kk}. More significant changes will be encountered in § 3.5.1. All initial bubble positions in § 3.5 will be selected in the close proximity of the wall in order to enable a study of the dependence of the cycle frequency on the distance to the wall.

The period of oscillation T_k and the initial deformation speed $\dot{b}_{k_{t=0}}$ are used to define a dimensionless 'natural frequency' ω_k by means of

$$\omega_k \overset{\text{def}}{=} 2\pi R_{t=0} \,/\, \left(T_k \left|\dot{b}_{k_{t=0}}\right|\right) = \tilde{\omega}_k R_{t=0} \,/\, \left|\dot{b}_{k_{t=0}}\right| , \tag{3.8}$$

with $\tilde{\omega}_k$ the radian frequency. The solution of (3.7) yields an angular frequency named $\omega_{k,Lamb}$ given by

$$\omega_{k,Lamb}^2 = (k-2)\cdot k \cdot (k+1)/\ We. \tag{3.9}$$

Here the initial Weber number We is defined by $We = R_{t=0}\rho_L \dot{b}_{k_{t=0}}^2/\sigma$. The expression for ω_k derived by Lamb (1932, equation (12), pp. 117 and 475, where $n = k-1$ and $S_n = P_n$) can be cast in the same form as (3.9). The above is therefore an alternative derivation of Lamb's radian frequency. It is noted that the dimensional radian frequency is given $\tilde{\omega}_{k,Lamb} = \sqrt{k(k-2)(k+1)\sigma/(\rho_L R_{t=0}^3)}$. A nonlinearized version of (3.7) for the case $k = 3$ will be given in § 3.5.

Examples of non-isotropic bubble deformation without a wall, that is, for $z = z_0 = \infty$, have been modelled with the models of § 2. The example of b_4-excitation is generated by choosing the initial velocity potential equal to a quadrupole potential with strength a_4 (BEM) or by selecting

$$\dot{b}_{4_{t=0}} \ = \ -4a_4 \, R_{t=0}$$

in the analytical method. This leads to an oscillating shape in which the coefficient of the third Legendre polynomial b_4 varies sinusoidally if the amplitude is small. The shape histories from both calculation methods are indistinguishable and the calculated angular frequency agrees with (3.9). A further comparison of the two methods will be given in § 3.5.2.

3.4. *Isotropically deforming spheres near but not very close to a wall*

In the presence of a wall, added mass coefficients other than ψ_{11} come into play if a spherical bubble is made to deform isotropically (expand or shrink). The added mass tensor of a spherical bubble near a wall was derived in previous work (Geld 2002). Use was made of an operator that was defined by the prescription

$$\tilde{G}_{ij} = -\delta_{ij} + \frac{i-1}{i}\frac{(i+j-2)!}{(i-1)!(j-1)!}(b_1/z)^{i+j-1},$$

where $b_1 = R$, the radius of the spherical bubble (see (2.1)). From $G_{mp} = b_1^{-p-1} m \tilde{G}_{mp}$ and $G_{pq}^{-1} = b_1^{p+1}\tilde{G}_{pq}^{-1}/q$ it is easily shown that (2.14) in this case reduce to

$$\begin{aligned} \alpha &= -1 - \frac{3}{2}\tilde{G}_{22}^{-1}, \\ \gamma_1 &= 6\tilde{G}_{21}^{-1}, \\ \psi_{11} &= 3 - 3\sum_{k=1}^{\infty} \tilde{G}_{k1}^{-1}(R/z)^k. \end{aligned} \tag{3.10}$$

This is exactly the result given by Geld (2002), where $tr(\beta) = \psi_{11}$ and $\psi_3 = -\gamma_1$, by definition. It is noted that Geld (2002, § 3) gives a rapidly converging series expansion,

as well as a good approximation, for the added mass coefficients of this case with the aid of the term $1/(1-(R/z)^3)$.

In this case of an oscillating spherical bubble near a plane wall, an extended Rayleigh–Plesset equation is derived from the Euler–Lagrange equation (2.16) for b_1, that is, the first row-equation of (2.19), in the following way. Since in this case $R = b_1$ it follows that

$$\frac{\partial \mathscr{V}_B}{\partial b_1} = 4\pi \left(b_1^2 + \sum_{j=3}^{\infty} \frac{1}{2j-1} b_j^2 \right) = 4\pi b_1^2, \tag{3.11a}$$

$$\frac{\partial A_B}{\partial b_1} = 4\pi \left(b_1(h_1+g_1) + \sum_{k=3}^{\infty} \frac{1}{2k-1} b_k(h_k+g_k) \right) = 8\pi b_1. \tag{3.11b}$$

The first row-equation of (2.19) reads

$$\begin{aligned} \frac{1}{3}\psi_{11} b_1 \ddot{b}_1 = &-\frac{1}{6}\gamma_1 b_1 \dot{U} + \frac{1}{\rho_L}(p_B - p_\infty) - \frac{2}{b_1}\frac{\sigma}{\rho_L} - \frac{1}{6}\dot{b}_1^2 b_1^{-2}\frac{\partial b_1^3 \psi_{11}}{\partial b_1} \\ &- \frac{2}{3} U \dot{b}_1 b_1 \frac{\partial \psi_{11}}{\partial z} + \frac{1}{6} U^2 b_1^{-2} \frac{\partial b_1^3 \alpha}{\partial b_1} - \frac{1}{3} U^2 b_1 \frac{\partial \gamma_1}{\partial z}. \end{aligned} \tag{3.12}$$

Not very close to a wall, see the definition below (3.4) in § 3.3, $\gamma_1 \simeq -3g^2$, $\alpha \simeq \frac{1}{2}$, $\psi_{11} \simeq 3(1+g)$ and it follows that

$$b_1 \ddot{b}_1 (1+g) + \dot{b}_1^2 \left(\frac{3}{2} + 2g \right) - \frac{1}{4} U^2 (1 - 8g^3) - \frac{1}{2} b_1 \dot{U} g^2 - 2U \dot{R} g^2 = \frac{p_B - p_\infty}{\rho_L} - \frac{2\sigma}{b_1 \rho_L}. \tag{3.13}$$

This is an extended Rayleigh–Plesset equation for a sphere near a plane wall. Other extensions will be derived below, (3.16) and (3.17). An equation similar to (3.13) for b_1 is (3.15) for b_3 that will be derived in § 3.5.1. The linearizing of (3.13) shows that the governing frequency is now in first-order approximation given by $(1 + R_{t=0}/z_{t=0})^{-1/2}\omega_{RP}$ because of the g-dependency of ψ_{11} (see (3.6)). Full deformation computations with both methods of § 2 show a good agreement with this frequency for many oscillation cycles further away from the wall, for example at $z_{t=0} = 30.R_{t=0}$, where $g_0 \overset{\text{def}}{=} R_{t=0}/z_{t=0} \simeq 0.03$. Note that even at this distance the phase shift induced by the correction $(1+g_0)^{-1/2}$ is considerable; without the correction the agreement would already be lost after one oscillation cycle.

Close to the wall, at $g_0 = 0.45$ for example, the frequency turns out not to be given by $(1+g_0)^{-1/2}\omega_{RP}$ anymore. Although in this case deformation becomes considerable, and coefficients b_3 and b_4 soon become as large as $b_1 - 1$, deformation is not the cause of the frequency shift. This is easily proven by a simulation with the analytical method in which all coefficients except b_1 are frozen to zero. The additional frequency change turns out to be a consequence of the induced motion U of the centre of the bubble. Velocity U is directed away from the wall, so an isotropically deforming bubble propels itself away from the wall. In § 3.5.7, a way to predict U will be presented and used to derive an improved approximation formula for the decreased frequency. Equation (3.13) turns out to be accurate also very close to the wall as long as Ug^4-terms are negligible.

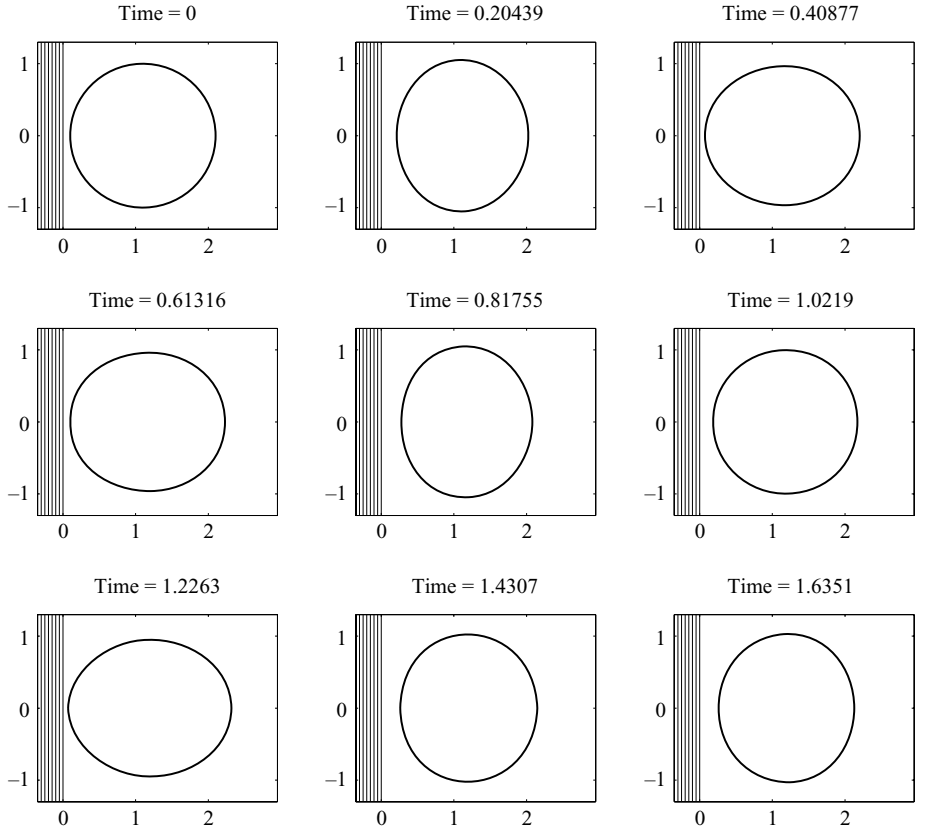

FIGURE 4. Bubble shape at equidistant time instants for $We = 0.12$. The wall is indicated by a set of straight parallel lines. Times are in units of $-R_{t=0}/(\mathrm{d}b_3/\mathrm{d}t)|_{t=0}$, distances in units of $R_{t=0}$. Initial deformation is according to what is defined as b_3-excitation in the text, with $\gamma = 1.4$ and $U|_{t=0} = 0$.

3.5. *Bubble motion induced by anisotropic large-amplitude deformation*

3.5.1. *An equation governing deformation of the b_3-mode near but not very close to a wall*

Let the bubble initially be a sphere with radius $R_{t=0}$ that starts to deform as (see (3.3))

$$R = R_{t=0}(1 + \tilde{\beta})\left\{1 + \tilde{f}_3 P_2\right\}, \tag{3.14}$$

with $\tilde{\beta} = (b_1 - R_{t=0})/R_{t=0}$ and $\tilde{f}_3 = b_3/b_1$ such that $\tilde{\beta}^2 \ll 1$ and $\tilde{f}_3^2 \ll 1$ at all times. Large amplitude implies shape deformations as depicted in figure 4. For ease of reference $\tilde{f}_3$ will be written as $\tilde{f}$ in the remainder of this section. In a similar way as the extended Rayleigh–Plesset equation (3.13) has been derived, the 3th row-equation of (2.19) can be reduced. Not very close to a wall (see the definition under (3.4) in § 3.3), this will yield an equation that governs b_3-changes. Using approximations for derivatives like, for example,

$$\frac{\partial G_{21}^{-1}}{\partial b_3} \simeq \frac{3}{10} g^2 b_1^2 \left(1 - \frac{3}{5}\tilde{f}\right)^{-2}\left(1 - \frac{4}{7}\tilde{f}\right),$$

the following approximations for derivatives of added mass coefficients are derived:

$$\frac{1}{\not\nu}\frac{\partial\gamma_1\not\nu}{\partial b_3} \simeq \frac{9}{5}\,b_1^{-1}\,g^2\left(1-\frac{31}{105}\tilde{f}\right)\left(1-\frac{3}{5}\tilde{f}\right)^{-1},$$

$$\frac{1}{\not\nu}\frac{\partial\gamma_3\not\nu}{\partial b_3} \simeq -\frac{6}{5}\,b_1^{-1}\,g^2\left(1+\frac{15}{42}\tilde{f}+\frac{33}{28}g^2\right),$$

$$\frac{1}{\not\nu}\frac{\partial\psi_{12}\not\nu}{\partial b_3} \simeq \frac{9}{10}\,b_1^{-1}\,g^2\left(1-\frac{3}{5}\tilde{f}\right)^{-2},$$

$$\frac{1}{\not\nu}\frac{\partial\psi_{32}\not\nu}{\partial b_3} \simeq \frac{3}{5}\,b_1^{-1}\,g^2\left(1+\frac{2}{7}\tilde{f}-\frac{3}{35}\tilde{f}^2+\frac{33}{14}g^2\right)\left(1-\frac{3}{5}\tilde{f}\right)^{-2}.$$

Terms with partial derivatives with respect to distance z, like $\partial\alpha/\partial z$, have turned out to be contributing only in close proximity of the wall. Not very close to the wall these terms are negligible and the following equation, dominating the time evolution of the anisotropic deformation component b_3 can be derived:

$$\begin{aligned}\frac{1}{6}\left(1+\frac{4}{7}\tilde{f}\right)b_1\ddot{b}_3 \approx\ & -\frac{1}{21}\dot{b}_3^2\left(1+\frac{199}{70}\tilde{f}\right)-\frac{1}{2}\dot{b}_1\dot{b}_3\left(1+\frac{3}{7}\tilde{f}\right)-\frac{1}{4}U^2\left(1+\frac{16}{35}\tilde{f}\right)\\ &+\frac{3}{4}\,U\,\dot{b}_1\,g^2\left(1+\frac{32}{105}\tilde{f}\right)-\frac{1}{2}\,U\,\dot{b}_3\,g^2\left(1+\frac{15}{42}\tilde{f}+\frac{33}{28}g^2\right)\\ &+\frac{1}{\rho_L}(p_B-p_{B,0})\tilde{f}-\frac{1}{\rho_L}\frac{2\sigma}{R_{t=0}}(2R_{t=0}/b_1-1)\tilde{f}\left(1-\frac{201}{392}\tilde{f}\right).\end{aligned} \tag{3.15}$$

The terms comprising the dimensionless distance squared g^2 are terms containing the velocity of the centroid U, and terms with U only contribute if the induced velocity U is non-negligible as compared to the imposed velocity $\dot{b}_3$. To assess the relative importance of terms in (3.15), simulations in § 3.5.2 and further will start at zero centre velocity, that is, $U_{t=0}=0$, whereas simulations in § 3.6 will have a non-zero initial centre velocity. In § 3.5.2 and further, initial velocity $\dot{b}_{k_{t=0}}$ will be taken such that $We=R_{t=0}\rho_L\dot{b}_{k_{t=0}}^2/\sigma=0.12$. Since (3.15) indicates no effect of the wall if $U=0$ and the bubble position is not in the vicinity of the wall, the initial position will be selected such that $g_{t=0}=R_{t=0}/z_{t=0}=1/2.2$, that is, only 10 % below the maximum value. Before discussing the results, in § 3.5.2 and further, some other considerations regarding (3.15) will be made.

Note that $p_B-p_{B,0}\approx -3\gamma\tilde{\beta}\,p_{B,0}$ and that (3.15) contains all dominant terms up to second-order perturbation quantities, that is, terms proportional to $\tilde{f}, \tilde{\beta}\tilde{f}, \tilde{f}^2, g^2\tilde{f}, g^2, g^4$. The linearizing of this equation leads to the oscillation frequency $\omega_{3,Lamb}$ as discussed in § 3.3. The $(p_B-p_{B,0})$ term is proportional to $\tilde{\beta}\tilde{f}$ and therefore of second order, while the surface tension term is of first order. This is the reason why all b_k-excitations ($k\geqslant 3$) are dominated by surface tension, while the isotropic Rayleigh–Plesset oscillatory motion (ω_{RP}) in § 3.1 was seen to be dominated by pressure.

The occurrence of the U^2 term on the right-hand side of (3.15) implies that if far away from any boundary a motion of the centroid in certain direction $\mathbf{e}_z$ is set in, the bubble interface described by $R(\vartheta)$ starts deforming according to $P_2(\cos\vartheta)=1/2(3\cos^2(\vartheta)-1)$, with ϑ the polar angle to $\mathbf{e}_z$. At the same time, also isotropic deformations start (see (3.13)). In the $U\dot{b}_1g^2$ term and the $U\dot{b}_3g^2$ term of (3.15) the distance to the wall appears, and these terms therefore only contribute in the presence of a wall. As noted in the above, these contributions will be investigated in § 3.6.

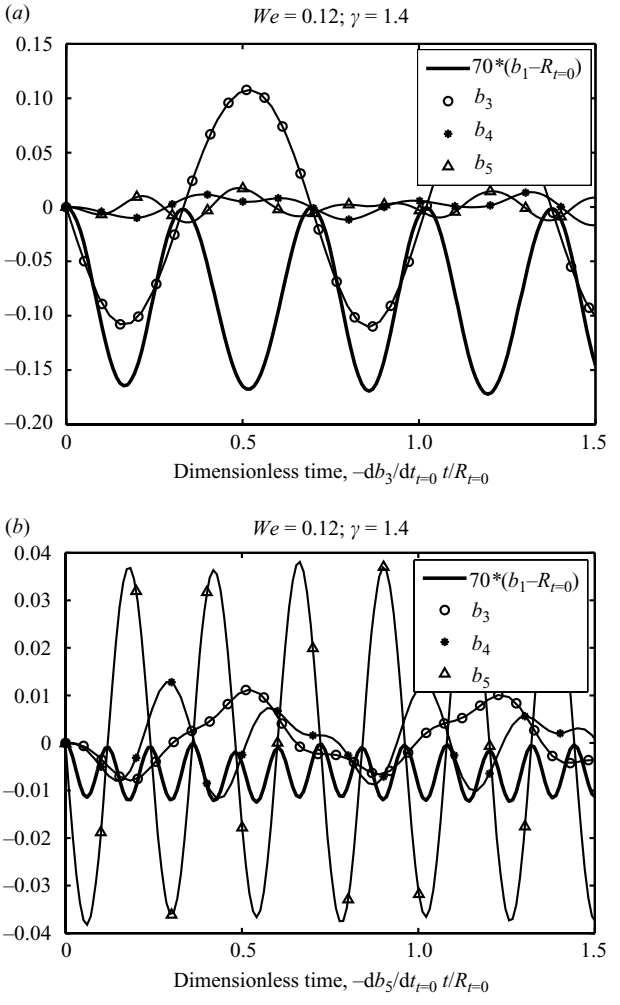

FIGURE 5. Histories of shape coefficients b_k for b_3-excitation (a), and b_5-excitation (b). $\gamma = 1.4$ and $We = 0.12$. The result for $\gamma = 0.1$ is indistinguishable.

3.5.2. *Effect of the wall on the angular frequency of b_k-excitation*

The effect of the wall on deformation and motion of a bubble starting from position given by $g_{t=0} = 1/2.2$ and starting with $U_{t=0} = 0$ has been investigated for $k = 3, 4, 5, 6, 7$. The shape history for $k = 3$ is shown in figure 4. The corresponding history of b_k-coefficients is shown in figure 5(a). In these figures, time is made dimensionless using $-\dot{b}_{3_{t=0}}/R_{t=0}$, where $\dot{b}_{3_{t=0}}$ is selected to be negative in order to have an initial induced velocity of the centroid away from the wall. The dimensionless times when $b_3 = 0$ are multiples of $\pi/\omega = 1/2|\dot{b}_{k,t=0}|T/R_{t=0}$ where ω is ω_3 (see (3.8)). The dimensionless frequency is initially about 10 % less than $\omega_{3,Lamb}$, which is 10 (see figure 5a: $2\pi/\omega \approx 0.7$ initially).

The frequency for b_5-mode excitation is in figure 5(b) observed to be also about 10 % less than $\omega_{5,Lamb}$, which equals $5\sqrt{30}$. Closing in to the wall reduces the frequency of b_k-excitation ($k > 2$), similar to the reduction of frequency of isotropically deforming spheres (see § 3.4). In his derivation of (3.9), Lamb took b_1 to be a constant

and independent of the equation of state of the bubble content, $p_B \mathscr{V}^{\gamma} = c$. The accuracy of this simplification will be studied in § 3.5.3 and § 3.5.5.

In general, coordinates b_m with m close to k experience with b_k-excitation a periodic motion with non-negligible amplitude. Comparison of figures 5(a) and 5(b) shows that the ratio of $\max(b_3)$ to $\max(b_5)$ is at least 20 % larger for b_3-excitation than the ratio of $\max(b_5)$ to $\max(b_3)$ for b_5-excitation; the maximum is here taken over several cycles of periodic motion. This coupling difference is due to the added mass tensor that is most conveniently described with the matrix $\boldsymbol{A}$ of (2.19). This coupling will be further discussed in § 3.5.3.

For the b_3-excitation case shown in figure 4 and figure 5(a), differences between the expansion method and those of the BEM have been studied in the following way. In both methods the time step has been chosen so small that further reduction of the time step results in negligible differences. In order to obtain the same initial condition in both methods the initial velocity potential of the expansion method has been used as initial condition in the BEM. In the expansion method 21 coefficients are used, whereas the number of collocation points used in the BEM is varied between 64 and 128. Figures 6(a) and 6(b) show the differences between both methods in two expansion coefficients, b_3 and b_7, as functions of time. These results show that the error due to the finite number of coefficients in the expansion method is negligibly small. Errors in the BEM decrease more than quadratically with the element size. For 128 collocation points the relative error in b_3 is of the order of 0.01 %, whereas the relative error in b_7 is smaller than 1 %.

As compared to the case where no wall is present, not only the frequency changes, but also a velocity of the centrepoint U is induced that is oscillating, see figure 7. The cycle-averaged value of U has a tendency to become negative eventually. This implies that despite the fact that initially the distance to the wall increases, the shape oscillations eventually drive the bubble towards the wall. This tendency is observed for excitation of any mode $k > 2$. Shape deformation and oscillation couple to volume oscillations, which cause the bubble to be attracted by its image in the wall. This will be further studied in § 3.5.6 and § 3.5.7.

The polytropic constant γ has usually values exceeding 1.0, and γ equals 1.0 for a constant bubble temperature. In this study, a typical value of an isentropic process with γ given by the ratio of the specific heats ($\gamma = 1.4$) is used, but for comparison also a value of 0.1 has been employed. By taking the exponent γ to be 0.1 the coupling between volume and pressure is obviously suppressed. However, this does not affect motion and velocities of the centrepoint. Figures 5 and 7 are the same for $\gamma = 0.1$, and similar observations are made for the histories of the added mass coefficients. An effect of γ is merely found for the accelerations, and in particular those of b_1, as will be discussed in § 3.5.5 and § 3.5.7. Since the computation time depends on the smallest time scales involved in the process, see § 3.1, and since the smallest time scale decreases with increasing γ, it is possible to reduce computation time of deformation histories by taking an artificially low value of γ. Only when coupling of volume and pressure are of interest this reduction of computation time is impossible.

3.5.3. *Coupling of motion and of deformation modes*

The coupling of deformation and motion of the centre-point is made by added mass coefficients, as the analytical method clarifies and is most clearly shown by (2.19). In derived equations such as (3.15), added mass coefficients are expressed in terms of generalized coordinates. Since these coordinates depend on time, so do the added mass coefficients (see figures 8 and 9). Initial conditions are the same as in § 3.5.2:

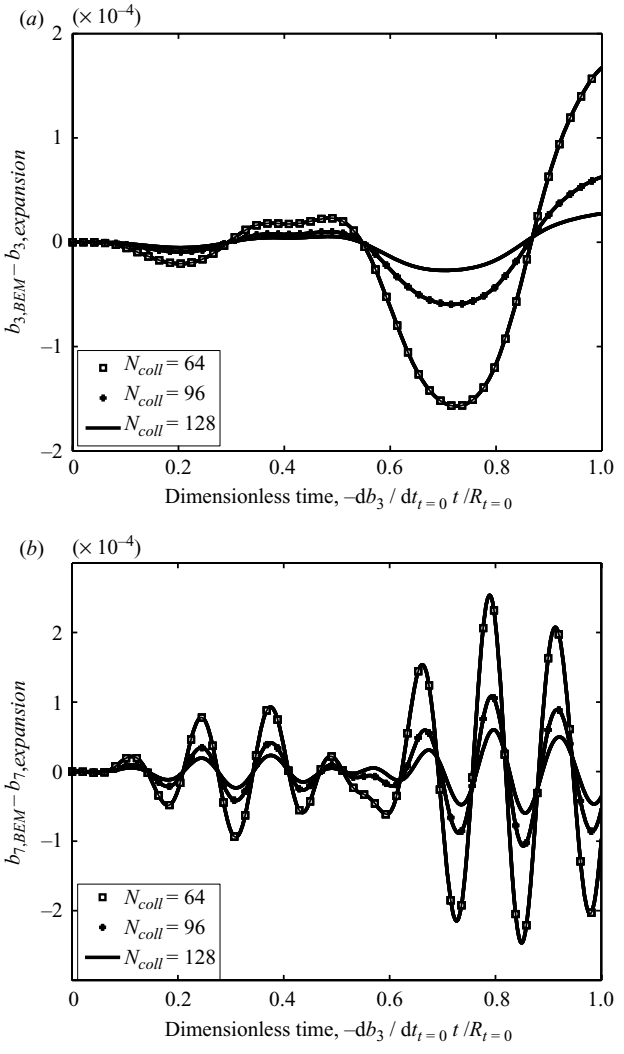

FIGURE 6. Differences in the value of b_3 (*a*) and b_7 (*b*) between a calculation with the expansion method and with BEM for b_3-excitation. $\gamma = 1.4$ and $We = 0.12$.

$z_{t=0} = 2.2R_{t=0}$ and $We = 0.12$. The value of the familiar added mass coefficient α is 0.5 for a sphere far away from the wall, of course, but about 0.7 and oscillating for a strongly deforming bubble in the vicinity of the wall (see figure 8). The amplitude of oscillation is larger for b_3 than for b_5-excitation (figure 8). Figure 9 shows some of the ψ_{1j} coefficients, j ranging from 3 to 5 and higher; these coefficients are clearly not constant in time. Coefficient ψ_{11}, on the contrary, is nearly constant in the corresponding cases, at a value close to 4.5. The value of ψ_{33} is oscillating around 0.25 with amplitude of about 0.04, and values of ψ_{ii}, $i > 3$, are about constant in time, positive and less than 0.2 and decreasing with increasing value of i. The cycle-averaged values of these ψ_{ij} parameters increase when the bubble gets very close to the wall. Apart from the amplitude of oscillation, time histories of the γ-added mass coefficients are similar (figure 8). The same holds for the time histories of ψ_{13} and ψ_{14}

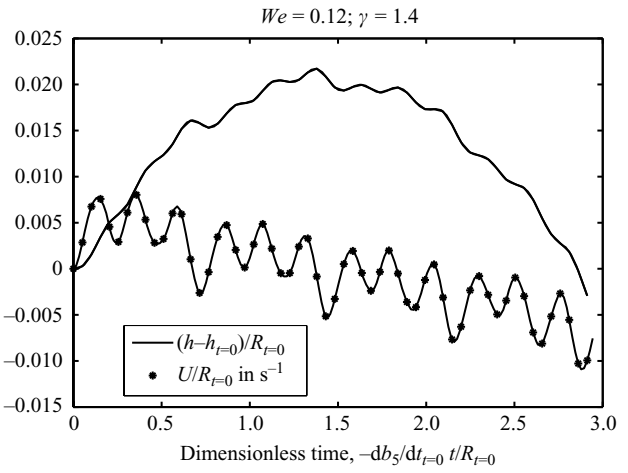

FIGURE 7. Trajectory and history of velocities of the centre point for b_5-excitation and $\gamma = 1.4$. The result for $\gamma = 0.1$ is exactly the same.

in, respectively, b_3 and b_4-excitation, as comparison of figures 9(a) and 9(b) shows. In both cases the value of ψ_{13} is oscillating around 0.25, but with different amplitude.

As a consequence, matrix $\boldsymbol{A}$ has a diagonal (ψ_{ii} and α) that is about constant in time in the deformation cases of this section. Values at the first row and first column ($\psi_{1j} = \psi_{j1}$) can be significant and are not constant, but fluctuate with minimum values close to zero (see figure 9). Also elements close to the diagonal are contributing at some times, but remaining values of $\boldsymbol{A}$ are usually negligible. There are times when matrix A is roughly a diagonal matrix and there are times when A is nearly zero anywhere outside the diagonal and outside the first column and row. This observation holds for excitation of any mode $k > 2$.

If the matrix $\boldsymbol{A}$ would *always* be a diagonal matrix, the equations of the generalized accelerations would be uncoupled. The importance of the first row and first column (corresponding to b_1 and z) shows that there is always coupling, for any b_k-excitation and for any generalized coordinate, with the b_1 parameter of spherical expansion or contraction. Because of this coupling, generalized coordinate b_1 is found to experience two superposed oscillations (see the typical result of figure 10). In histories of generalized coordinates shown in figure 5 the high, ω_{RP}-like, frequency component cannot be distinguished. For this reason, figure 10 shows the history of the acceleration $\ddot{b}_1$. Far away from the wall, the high frequency is the frequency ω_{RP} given by (3.2). In the example of b_5-excitation these oscillations are superposed on a frequency that is twice the natural frequency of b_5, ω_5 (see (3.8) and (3.9)). The reason of this low-frequency doubling of ω_5 in b_1, which is also clearly observed in figure 5, is investigated in § 3.5.5 with the aid of a Rayleigh–Plesset equation that is extended with terms to account for deformation.

3.5.4. *A Rayleigh–Plesset equation with deformation*

With only spherical deformation, the first row-equation of (2.19) would yield the extended Rayleigh–Plesset equation (3.13) (see § 3.1). In the case of full deformation, the first row-equation of (2.19) is found to encompass not only $\ddot{b}_1$ but all other generalized accelerations. This Euler–Lagrange equation, a further extension of the

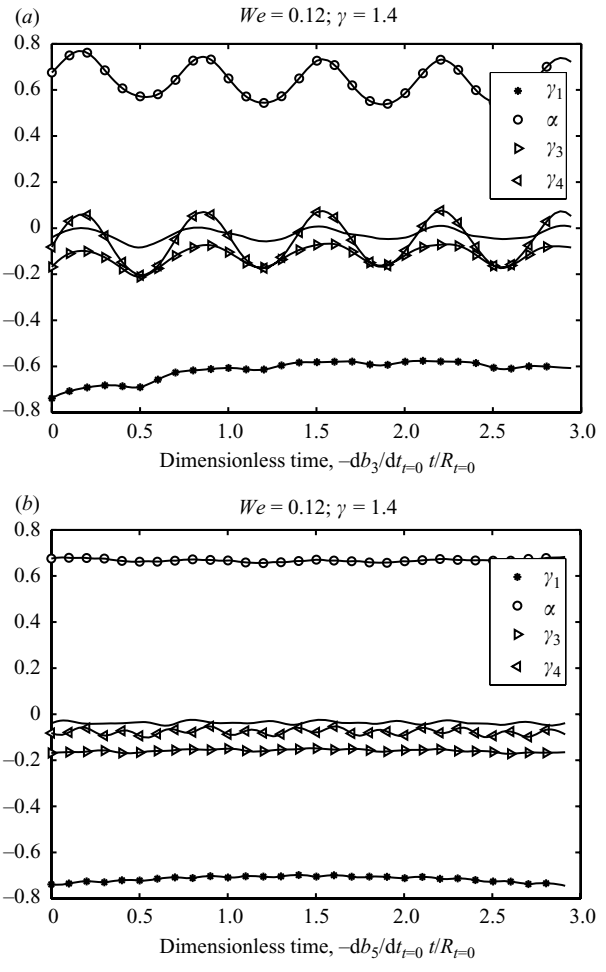

FIGURE 8. Histories of added mass coefficients α and γ_j for b_3-excitation (a), and b_5-excitation (b). $We = 0.12$ and $\gamma = 1.4$. The plain solid line corresponds to γ_5.

Rayleigh–Plesset equation, can be written as:

$$
\begin{aligned}
&2\psi_{11}\mathscr{V}\ddot{b}_1 + \gamma_1\mathscr{V}\dot{U} + 2\mathscr{V}\sum_{k=3}^{\infty}\psi_{k1}\ddot{b}_k \\
&\quad = 2Q_1/\rho_L - \dot{b}_1^2\,\frac{\partial\psi_{11}\mathscr{V}}{\partial b_1} - 2\dot{b}_1\left\{2U\mathscr{V}\frac{\partial\psi_{11}}{\partial z} + \sum_{k=3}^{\infty}\dot{b}_k\,\frac{\partial\psi_{11}\mathscr{V}}{\partial b_k}\right\} + U^2\,\frac{\partial\alpha\mathscr{V}}{\partial b_1} \\
&\qquad + U\sum_{k=3}^{\infty}\dot{b}_k\,\frac{\partial\gamma_k\mathscr{V}}{\partial b_1} + \sum_{k,m=3}^{\infty}\dot{b}_k\dot{b}_m\,\frac{\partial\psi_{mk}\mathscr{V}}{\partial b_1} - 4U\mathscr{V}\sum_{k=3}^{\infty}\dot{b}_k\,\frac{\partial\psi_{k1}}{\partial z} \\
&\qquad - 2U^2\,\mathscr{V}\frac{\partial\gamma_1}{\partial z} - 2\sum_{k,m=3}^{\infty}\dot{b}_k\dot{b}_m\,\frac{\partial\psi_{m1}\mathscr{V}}{\partial b_k} - U\sum_{k=3}^{\infty}\dot{b}_k\,\frac{\partial\gamma_1\mathscr{V}}{\partial b_k}.
\end{aligned}
\tag{3.16}
$$

The generalized force Q_1 is given by (2.17) with derivatives given by the equalities on the left-hand side of (3.11), for example. Note that explicit analytical expressions exist

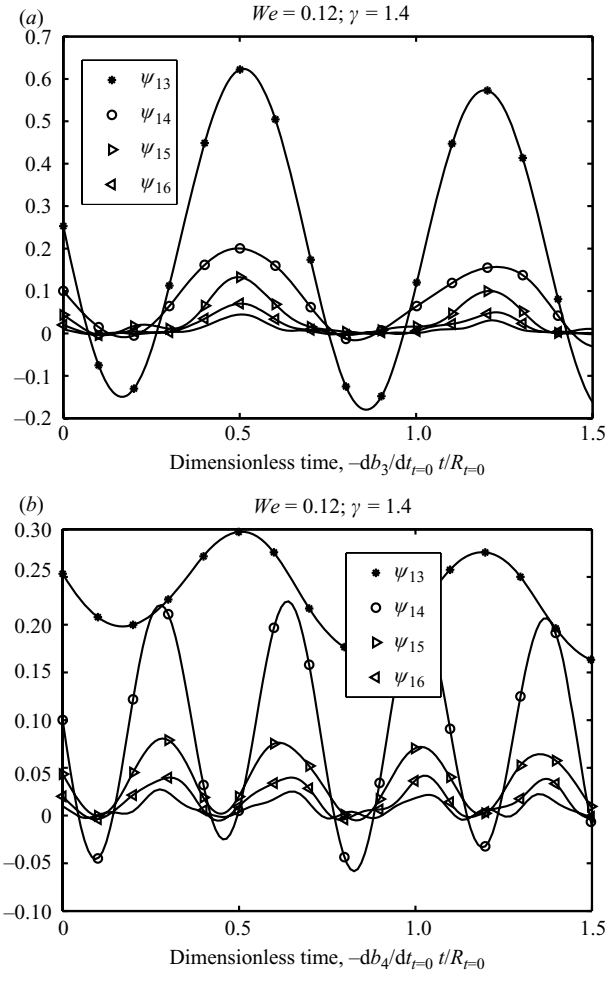

FIGURE 9. Histories of added mass coefficients ψ_{1j} for b_3-excitation (a), and b_4-excitation (b). $We = 0.12$ and $\gamma = 1.4$. The plain solid line corresponds to ψ_{17}.

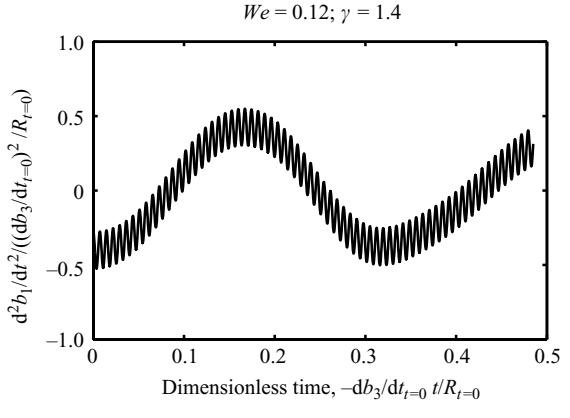

FIGURE 10. History of acceleration of the first generalized coordinate b_1 corresponding to isotropic deformation for b_3-excitation. $We = 0.12$ and $\gamma = 1.4$. The frequency of the high-frequency component increases with increasing γ.

for all derivatives in (3.16) (see § 2.2). The classical Rayleigh–Plesset equation was used in many applications, viz. boiling and cavitation (Brennen 1995), Bjerknes attraction (Prosperetti 1984) and generation of sound (Versluis *et al.* 2000). No equivalent or extended Rayleigh–Plesset equation to account for non-spherical deformation close to a wall has been found in the literature, despite its importance in the aforementioned applications.

The simplification of (3.16) for b_3-excitation is analysed away from the wall in § 3.5.5, leading to (3.20).

3.5.5. *Frequency-doubling of b_1 component, away from the wall*

In case of b_3-excitation as defined in § 3.3, each sum $\sum_{k=3}^{\infty}$ in (3.16) reduces to the case $k=3$ only. With $\tilde{f}=b_3/b_1$ the volume is then given by $\mathscr{V}=\frac{4}{3}\pi b_1^3(1+\frac{3}{5}\tilde{f}^2+\frac{2}{35}\tilde{f}^3)$. This yields away from the wall and for $U \ll \dot{b}_3$ and $\dot{U} \ll \ddot{b}_3$:

$$2\psi_{11}\ddot{b}_1 + 2\psi_{31}\ddot{b}_3 \approx 6\frac{p_B - p_\infty}{\rho_L}\left(b_1^2 + b_3^2/5\right)b_1^{-3} - 12\frac{\sigma}{\rho_L}b_1^{-2} + \dot{b}_3^2\,\frac{1}{\mathscr{V}}\frac{\partial \psi_{33}\mathscr{V}}{\partial b_1} - 2\dot{b}_3^2\,\frac{1}{\mathscr{V}}\frac{\partial \psi_{31}\mathscr{V}}{\partial b_3}. \quad (3.17)$$

The following approximations are derived for the partial derivatives of added mass coefficients remaining in (3.17):

$$\frac{1}{\mathscr{V}}\frac{\partial \psi_{33}\mathscr{V}}{\partial b_1} \simeq \frac{3}{5}b_1^{-1}\left(1+\frac{3}{7}\tilde{f}\right)\left(1+\frac{3}{5}\tilde{f}^2+\frac{2}{35}\tilde{f}^3\right)^{-1}, \quad (3.18a)$$

$$\frac{1}{\mathscr{V}}\frac{\partial \psi_{31}\mathscr{V}}{\partial b_3} \simeq b_1^{-1}\left(1+\frac{1}{7}\tilde{f}\right)\left(1+\frac{3}{5}\tilde{f}^2+\frac{2}{35}\tilde{f}^3\right)^{-1}, \quad (3.18b)$$

while the added mass coefficients in (3.17) away from the wall can be approximated as follows:

$$\psi_{11} \simeq 3\left(1+\frac{3}{5}\tilde{f}^2+\frac{2}{35}\tilde{f}^3\right)\Big)^{-1}, \quad (3.19a)$$

$$\psi_{31} = \psi_{13} \simeq \tilde{f}\left(1+\frac{4}{7}\tilde{f}\right)\left(1+\frac{3}{5}\tilde{f}^2+\frac{2}{35}\tilde{f}^3\right)^{-1}. \quad (3.19b)$$

The b_1 equation (3.17) can with (3.18*b*) and (3.19*b*) be written as

$$b_1\ddot{b}_1 + \frac{1}{3}b_3\ddot{b}_3\left(1+\frac{3}{7}\tilde{f}\right) \simeq \left\{\frac{p_B - p_\infty}{\rho_L}(1+\tilde{f}^2/5) - 2\frac{\sigma}{\rho_L}b_1^{-1}\right\}\left(1+\frac{3}{5}\tilde{f}^2 + \frac{2}{35}\tilde{f}^3\right) + \dot{b}_3^2\left(-\frac{7}{30}-\frac{1}{105}\tilde{f}\right), \quad (3.20)$$

where the first term is reminiscent of the first term in (3.13) and no g-terms appear because of the assumption made to be away from the wall.

Away from the wall, coefficient b_3 in a b_3-excitation turns out to be well described by

$$b_3 = -\beta R_{t=0}\sin(\tilde{\omega}_3 t) \quad (3.21)$$

with $\tilde{\omega}_3$ corresponding to $\omega_{3,Lamb}$, that is, $\tilde{\omega}_3 = \omega_{3,Lamb}|\dot{b}_{3_{t=0}}|/R_{t=0}$, and β a small parameter. For constant σ, ρ_L and $R_{t=0}$, $We \propto \dot{b}_0^2$, $\omega_{3,Lamb} \propto 1/|\dot{b}_3|_{t=0}$, $\tilde{\omega}_3$ is constant and $\beta = 1/2|\dot{b}_3|_{t=0}$. Typical values are $We = 0.12$ and $\beta = 0.1$ (see also figure 5). Let

it now be assumed that b_1 can be expanded in the following series:

$$b_1 = b_{1,0} + \varepsilon b_{1,1} + \varepsilon^2 b_{1,2} + \cdots$$

with $b_{1,0} = R_{t=0}$ and with ε a small parameter, $\varepsilon \ll 1$. If will follow from equation (3.20) that ε is indeed a small parameter if β is. With

$$\omega_{RP}^2 = \frac{3\gamma p_\infty}{\rho_L b_{1,0}^2} + \frac{2(3\gamma - 1)\sigma}{\rho_L b_{1,0}^3},$$

see also (3.2), it can now be shown that the generalized force, Q_1, in first order approximation is given by

$$Q_1 \simeq -\left(\frac{b_1 - b_{1,0}}{b_{1,0}} + \frac{1}{5}\beta^2 \sin^2(\tilde{\omega}_3 t)\right) 4\pi\, b_{1,0}^4\, \omega_{RP}^2\, \rho_L. \tag{3.22}$$

The b_1 equation (3.20) can with (3.22) be written as

$$b_1\ddot{b}_1 + \frac{1}{3}b_3\ddot{b}_3 \simeq -\left\{\frac{b_1 - b_{1,0}}{b_{1,0}} + \frac{1}{5}\beta^2 \sin^2(\tilde{\omega}_3 t)\right\} b_1^{-2}\, b_{1,0}^4\, \omega_{RP}^2 + \dot{b}_3^2\left(-\frac{7}{30} + \frac{1}{105}b_3/b_1\right). \tag{3.23}$$

It follows that $b_{1,1}$ is given by

$$\varepsilon b_{1,1} = \tilde{A} R_{t=0}\{\cos(2\tilde{\omega}_3 t) - 1\} + B R_{t=0}\omega_{RP}^{-2}\,(\cos(\omega_{RP} t) - 1) \tag{3.24}$$

with

$$\tilde{A} = \frac{1}{10}\beta^2 \frac{\{\omega_{RP}^2 - 3\tilde{\omega}_3^2\}}{\{\omega_{RP}^2 - 4\tilde{\omega}_3^2\}} \quad \text{and} \quad B = \frac{1}{20}\beta^2 \tilde{\omega}_3^2 \frac{\{\omega_{RP}^2 + 4\tilde{\omega}_3^2\}}{\{\omega_{RP}^2 - 4\tilde{\omega}_3^2\}}. \tag{3.25}$$

Parameter ε turns out to be proportional to β^2, so small if $\tilde{\omega}_3 \ll \omega_{RP}$, which is normally the case. Since b_1 occurs in the governing equation of b_3 (see (3.15)), the proportionality of ε with β^2 explains why (3.21) gives such a good description of b_3. Coefficient $\tilde{A}$ being a constant, solution (3.24) clearly shows the frequency doubling that is manifest in b_1 histories of the numerical solutions of b_k-excitations. It is noted that Prosperetti (1977) showed that for oscillatory motion described by (3.21) radiation and thermal losses are proportional to β^4, so negligible with the present assumptions.

It is easy to rewrite (3.24) into

$$\varepsilon b_{1,1}/R_{t=0} = \beta^2 \frac{1}{10}\left(\{\omega_{RP}^2 - 3\tilde{\omega}_3^2\}/\{\omega_{RP}^2 - 4\tilde{\omega}_3^2\}\right) 2\sin\left(\frac{1}{2}(2\tilde{\omega}_3 + \omega_{RP})t\right) \times \sin\left(\frac{1}{2}(\omega_{RP} - 2\tilde{\omega}_3)t\right) + \beta^2 \frac{1}{10}\left\{1 + \frac{1}{2}\frac{\tilde{\omega}_3^2}{\omega_{RP}^2}\right\}(\cos(\omega_{RP} t) - 1), \tag{3.26}$$

which has an amplitude that becomes large if $\omega_{RP}/2$ approaches $\tilde{\omega}_3$. This is a nice extension of the work of Longuet-Higgins (1989*a*), who tried to explain the source of underwater noise at sea (see also Longuet-Higgins 1989*b*,*c*). Longuet-Higgins showed that each oscillation with amplitude β at the frequency of a linear fundamental mode produces oscillations that behave at a distance just as those of what he calls the breathing mode, which is the fundamental radial mode with radian frequency ω_{RP}, and with an amplitude proportional to β^2. This is the frequency doubling observed in the above. Longuet-Higgins merely derived the component with $\cos(2\tilde{\omega}_3 t)$ in solving his equation (6.23) with a velocity potential given by $Z R_{t=0} \sin(2\tilde{\omega}_3 t)/r$.

It can, however, easily be shown that $ZR_{t=0}\sin(2\tilde{\omega}_3 t)/r + QR_{t=0}\sin(2\omega_{RP}t)$ is also a family of solutions of his equation (6.23), for any value of Q. Longuet-Higgins took Q to be zero. In his approach, three parameters are perturbed simultaneously. In our approach, two of his parameters (velocity potential and pressure) are expressed in terms of the other, which is interface deformation as described by the generalized coordinates.

If $\tilde{\omega}_3$ is close to $\omega_{RP}/2$, the amplitude of the oscillatory component with $\tilde{\omega}_3$ in (3.26) reaches a maximum in the typical time $\pi/(\omega_{RP} - 2\tilde{\omega}_3)$. However, way before that time ε is found not to be small anymore. The coupled equations for b_1 and b_3 need to be solved together in that case. In many practical cases, ω_{RP}^2 exceeds $\tilde{\omega}_3^2$ by far, while relative volume changes are less than 0.001. In these cases part of the solution of Tsamopoulos & Brown (1983) is recovered. These authors also found an isotropic component with amplitude $(b_3/R_{t=0})^2/5$, in their equation (56*a*) combined with their definition 12. This part of the frequency doubling is apparently not connected to volume changes, since Tsamopoulos and Brown did not employ an equation of state and assumed the bubble to have a constant volume. Further comparison with the results of these authors is not only hampered by their using a different equation of state, but mostly by their assumption of a fully periodic motion and therefore not specifying the initial shape precisely. The decrease in frequency with amplitude, which they and other authors found in the absence of a wall, is recovered in our approach with a realistic equation of state.

Summarizing, in the extended Rayleigh–Plesset equation (3.17) terms with $\dot{b}_3^2$ are significant whenever $\dot{b}_3$ is not close to zero. Shape expansion coefficient $\dot{b}_3$ is oscillating around zero at about $\omega_{3,Lamb}$ (figure 5*a*), and a quadratic term yields a frequency doubling. Since velocity U is also oscillating at about the natural frequency $\omega_{3,Lamb}$ (figure 7), the terms with U^2 and $U\dot{b}_3$ in (3.16) add to the frequency-doubling observed in b_1. The importance of a term with U^2 can be judged from an analysis of the contributions to the kinetic energy T because T contains the term αU^2. Since the history of the kinetic energy budget also reveals the coupling of shape deformation to motion of the centrepoint, it is studied in § 3.5.6 before in § 3.5.7 the second row-equation of (2.19) is analysed.

3.5.6. *Energy transfer*

In figure 11, the history of kinetic energy T, (see (2.13)) is compared with its initial value, T_0, and with the potential energy change history of $\sigma(A_B - A_{B,0})$, where $A_{B,0}$ is the initial bubble surface area. Integration of

$$\frac{\mathrm{d}T}{\mathrm{d}t} = \sum_j (p_B - p_\infty)\frac{\partial \mathscr{V}}{\partial q_j}\dot{q}_j - \sigma\frac{\mathrm{d}A_B}{\mathrm{d}t} \tag{3.27}$$

easily shows that $T + \sigma A_b + p_\infty \mathscr{V} - p_{B,0}\mathscr{V}_0^\gamma \frac{1}{1-\gamma}\mathscr{V}^{1-\gamma}$ is constant. The pressure-related energy part contributes to the energy budget of the high-frequency oscillations of §§ 3.1, 3.3 and 3.4, for example, but turns out to be negligible in the results of figure 11. The volume oscillations induced by shape deformation cause the bubble to move to the wall, but at a longer time scale.

Comparison of figure 11 with figure 5(*a*) shows that kinetic energy T is oscillating at twice the natural frequency $\omega_{3,Lamb}$ with non-constant amplitude. Kinetic energy is never zero, but as in any undamped spring-mass system there is continuous transfer of kinetic energy to potential energy and vice versa. In the present deformation case all potential energy is in the enlargement of the area of the gas–liquid interface

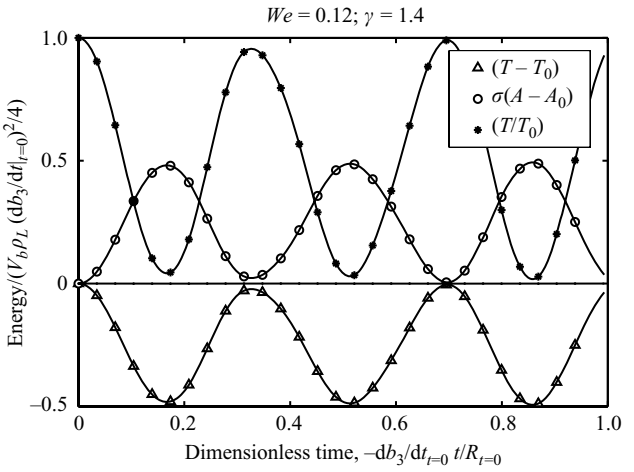

FIGURE 11. Histories of energy contributions for b_3-excitation. The kinetic energy has initial value T_0 and $V_b = \mathscr{V}$. The virtual mass $1/2\rho_L\mathscr{V}$ and the initial deformation velocity have been used for scaling. $We = 0.12$ and $\gamma = 1.4$. The plain solid line is the sum of $T - T_0$ and $\sigma(A_B - A_{B,0})$.

(see figure 11). At initial time zero, $U = 0$ and only the ψ_{33} term is contributing to T (see (2.13)). Since $\dot{b}_3 < 0$, the γ_3 term proportional to both $\dot{b}_3$ and U on the right-hand side of (2.13) starts decreasing the value of T at subsequent times. In the first crest of potential energy, at around 0.17 in dimensionless time units, $\dot{b}_3 = 0$ and the small value of T corresponds to the small value of U^2 at that time. At the subsequent maximum value of T, at time 0.33, $\dot{b}_3$ is positive and possesses a maximum value (figure 5*a*) while U is close to its maximum (positive) value. Nearly all kinetic energy is recovered, while the remainder is stored in $\sigma(A_B - A_{B,0})$ (see figure 11). One period of oscillation of T later, both U and $\dot{b}_3$ are negative and possess minimum values. Each time the main deformation amplitude reaches its maximum value ($\dot{b}_3 = 0$), kinetic energy in the fluid (T) reaches a minimum value that is fully determined by the kinetic energy of the motion of the centre point of the bubble (αU^2). The governing equation of this motion is studied in the next § 3.5.7.

3.5.7. *Governing equation for motion of the centroid*

The motion of the centrepoint would be fully determined by the second row-equation of the matrix equation in A, (2.19), if the motion of all generalized coordinates would be uncoupled. Since the coupling of U with coordinates other than b_3 and b_4 is weak, see the low values of the coupling constants $\gamma_4, \gamma_5, \ldots$ in figure 8, and since accelerations $\ddot{b}_1$ are found to be small, the second row-equation of (2.19) is expected to govern the motion of the centrepoint. Its main contributions will now be analysed.

The corresponding Euler–Lagrange equation can be given the form

$$\frac{1}{\mathscr{V}}\frac{\mathrm{d}}{\mathrm{d}t}\{2\alpha U\mathscr{V}\} + \frac{1}{\mathscr{V}}\frac{\mathrm{d}}{\mathrm{d}t}\left(\mathscr{V}\sum_m^\infty \gamma_m \dot{b}_m\right) - 2\sum_{i,j}^\infty \dot{b}_i\dot{b}_j\frac{\partial\psi_{ij}}{\partial z} + -2U\sum_m^\infty \dot{b}_m\frac{\partial\gamma_m}{\partial z} \simeq 0, \quad (3.28)$$

where the approximate sign is to account for the neglect of the term $-2U^2\partial\alpha/\partial z$ on the left-hand side of this equation. This term is found to be negligible for deformation-driven bubble motion at all times. The histories of three remaining terms

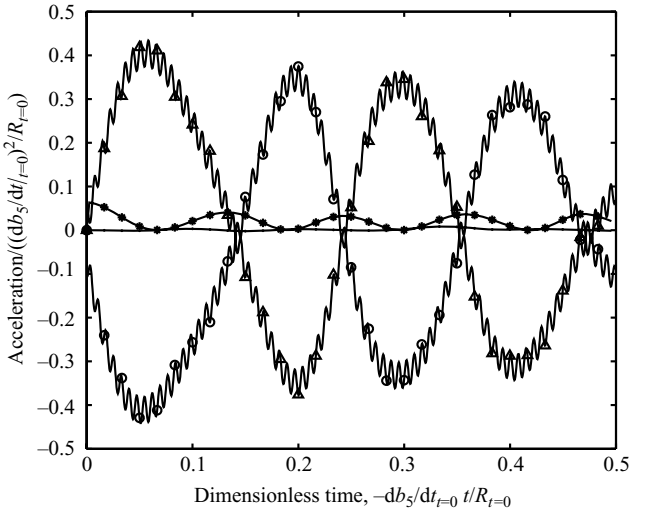

FIGURE 12. Histories of dimensionless accelerations for b_5-excitation. $We = 0.12$ and $\gamma = 1.4$. Triangels denote $(1/\mathscr{V})(d/dt)\{2U\alpha\mathscr{V}\}$, open circles denote $(1/\mathscr{V})(d/dt)\{\mathscr{V}\sum_m^\infty \dot{b}_m\gamma_m\}$, solid dots denote $-2\sum_{ij}\dot{b}_i\dot{b}_j(\partial\psi_{ij}/\partial z)$. The main contributions to the second Lagrange–Hamilton equation are shown. The plain solid line is the sum of the three contributions.

are for b_5-excitation plotted in figure 12. The high-frequency oscillation component related to ω_{RP} is clearly visible in the generalized accelerations shown. The fourth term on the left-hand side of (3.28) can be neglected in first-order approximation (see the solid line in figure 12). Integration of (3.28) then yields

$$U \simeq (\alpha\mathscr{V}U)|_{t=0}/(\alpha\mathscr{V}) + \int_0^t \mathscr{V}\sum_{i,j}^{\infty}\dot{b}_i\dot{b}_j\,\frac{\partial\psi_{ij}}{\partial z}\,\mathrm{d}t'/(\alpha\mathscr{V}) + \left\{(\gamma_1\dot{b}_1)\big|_{t=0} + \sum_{j=3}^{\infty}(\gamma_j\dot{b}_j)\big|_{t=0} - \gamma_1\dot{b}_1 - \sum_{j=3}^{\infty}\gamma_j\dot{b}_j\right\}\Big/(2\alpha), \quad (3.29)$$

where the terms are evaluated at time t unless denoted otherwise. The volume ratio $\mathscr{V}_{t=0}/\mathscr{V}$ in the third term on the right-hand side is neglected since this ratio is about 10^{-4} % maximum in all simulations of § 3.5. In all cases of the present section, $U_0 \overset{\text{def}}{=} U|_{t=0} = 0$, and the first term on the right-hand side of (3.29) is zero. It is retained here for ease of reference. The integral in the second term on the right-hand side is approximately given by $\int_0^t \mathscr{V}\sum_j^\infty \dot{b}_j^2\,\frac{\partial\psi_{jj}}{\partial z}\,\mathrm{d}t$. Because of the negative sign of each derivative $\partial\psi_{jj}/\partial z$ this second term on the right-hand side is always negative. Also in the simulation of figure 12 this term appears to be negative always. This negative sign explains the following general trend that has been observed in all simulations. Finite-amplitude excitation of any mode b_k in the presence of a wall always leads to motion of the bubble towards the wall (see figure 7). If the sign of the initial deformation velocity is taken to be positive, initially induced velocities U are negative and the bubble merely reaches the wall in a shorter time span. This tendency is a long-term trend that follows from the second term on the right-hand side of (3.29). If this term were left out, the resulting error in U would be about 10 % after a quarter of a cycle of ω_5.

The third term on the right-hand side of (3.29) clearly explains why velocity U has an oscillatory component at about the natural frequency $\omega_{k,Lamb}$ of $\dot{b}_k$ (see figures 7 and 5*b*). It turns out that for the deformation simulations of b_k-excitations of § 3.5 it is possible to replace the sum $\sum_{j=3}^{\infty}$ in this third term by the $\sum_{j=k-1}^{k+1}$ without affecting deformation predictions much.

Equation (3.29) allows the following derivation of the cycle frequency of isotropic oscillation near a wall (see also § 3.4). Since $\dot{b}_1^2$ terms do not contribute in (3.13), $\dot{U}$ on the left-hand side of this equation can be approximated with $-\gamma_1 \ddot{b}_1/(2\alpha)$ (see (3.29)). With the already used approximation $-3g^2$ for γ_1 in (3.13), the following equation for the cycle frequency ω is then easily derived:

$$\omega^2 = \omega_{RP}^2 \Big/ \left\{ 1 + g_0 - \frac{3}{2} g_0^4 \Big/ (2\alpha) \right\}. \tag{3.30}$$

The value of α is approximately 0.7 close to a wall, and this yields the following approximation of ω: $(1+g_0-\frac{3}{2.8}g_0^4)^{-1/2}\omega_{RP}$. Full deformation computations with both methods of § 2 show a good agreement with this frequency for many oscillation cycles close to the wall.

The frequency $(1+g_0-\frac{3}{2.8}g_0^4)^{-1/2}\omega_{RP}$ is somewhat reduced as compared to ω_{RP}. The physical explanation of the decrease in oscillation frequency of isotropic expansion when the distance of the bubble to the wall is reduced is the increase of added mass (ψ_{11}). Liquid in between bubble and wall needs to be directed away, that is, needs to be accelerated in a direction parallel to the wall. The fluid that is pushed away from the half of the sphere that faces the wall needs to find its way through a surface area that at distance r from the centre of the sphere is considerably smaller than $2\pi r^2$. Thus, acceleration is required that leads to more kinetic energy which means increased added mass (see the defining equation (2.13)). The higher the mass of a pendulum, the lower its frequency.

A bubble that is close to a wall can only get away from this wall either if its deformation has a strong isotropic component or if its centroid possesses a substantial positive velocity U. The latter case is therefore investigated in § 3.6.

3.6. *Bubble deformation induced by motion perpendicular to a plane wall*

Another generic test case is that of an initially spherical bubble set into motion away from the wall at arbitrary Weber number. The corresponding Weber number is defined as

$$We \stackrel{\text{def}}{=} \rho_L U_0^2 R_{t=0}/\sigma,$$

where U_0 is the initial velocity of the bubble. If the Weber number is small, surface tension tends to prevent large deformation of the bubble. As shown in § 3.5.7, an initially high positive value of the velocity of the centroid is the only way for a strongly anisotropically deforming bubble to escape from the influence of the wall and get at a distance from the wall.

3.6.1. *Effect of Weber number*

In the first example, *We* is taken to be 0.12, which corresponds to an air bubble in water at room temperature with radius of 1 mm and initial velocity of 0.1 m s^{-1}. The pressure at infinity equals atmospheric pressure. The initial distance of the bubble centroid to the wall, $z_0/2$, is again chosen to be $1.1R_{t=0}$. The initial pressure inside the bubble is chosen such that the bubble would be in equilibrium if U_0 would be zero. The BEM starts from an initial velocity potential generated by a dipole with strength $1/2U_0R_{t=0}$ at the bubble centre plus a dipole with the same strength and

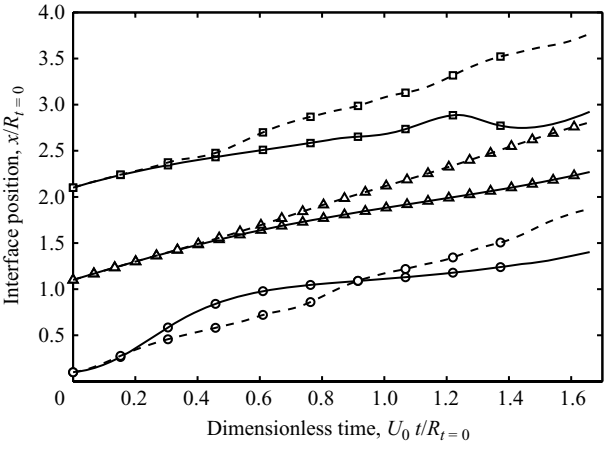

FIGURE 13. Positions of the leading edge (circle), centroid (triangle) and trailing edge (square box); solid lines: $We = 1.2$; dashed lines: $We = 0.12$.

opposite direction at the centre of the bubble mirror image. The analytical method starts, equivalently, from a spherical shape and from a given velocity potential with coefficients a_m that correspond to two dipoles, each with strength as used in the BEM. Then the corresponding velocities $\{\dot{b}_m\}$ and U are computed by solving (2.9), with $a_2 = 1/2U_0R_{t=0}$, $0 = a_1 = a_3 = a_4 = a_5 = \ldots$. Although it is somewhat more work in the analytical approach, this initialization greatly facilitates the BEM computation. Clearly, the initial condition is a mixed one of both deformation and velocity of the centre U, although U is by far the most important generalized velocity.

In figure 13 the time evolution of the positions of the leading edge, centroid and trailing edge is shown by dashed lines. It can be seen that the velocity of the centroid is practically constant and that the deformation of the bubble is small. As a further illustration, the bubble shape at various times is shown in figure 14.

In the next example the only difference with the previous example is that the Weber number is increased to $We = 1.2$. This implies that the deformation restrictive influence of surface tension is less. The time evolution of the positions of leading edge, bubble centre of mass and trailing edge are shown in figure 13 by solid lines. By comparing the two cases two phenomena are noticeable. First, the higher Weber number corresponds to larger deformations, which can be deduced from the variations in distance between leading and trailing edge, as well as from the shape history of figure 15. Second, the velocity of the bubble centroid gets smaller for the higher Weber number. This phenomenon is explained below.

3.6.2. *The reason why velocity decreases with increasing deformation*

Figure 16 shows that in the deformation case corresponding to $We = 1.2$ at least about twenty generalized coordinates $(b_1, b_3, b_4, \ldots)$ are required to describe the shape at all times. This figure shows both the distance to the wall and the dimensionless time of passing. The changes of the amplitudes $\{b_i\}$ at times later than those shown in figures 16 and 15 are comparable to those seen in figure 16. Figures 17 and 18 show the histories of the dominant added mass coefficients, α, γ_j and ψ_{1m}, for the case $We = 1.2$, as well as the corresponding distances from the wall. At large distance from the wall the value of α of a sphere is 0.5. Without deformation, the value of α would be monotonically decreasing with increasing distance from the wall (Geld

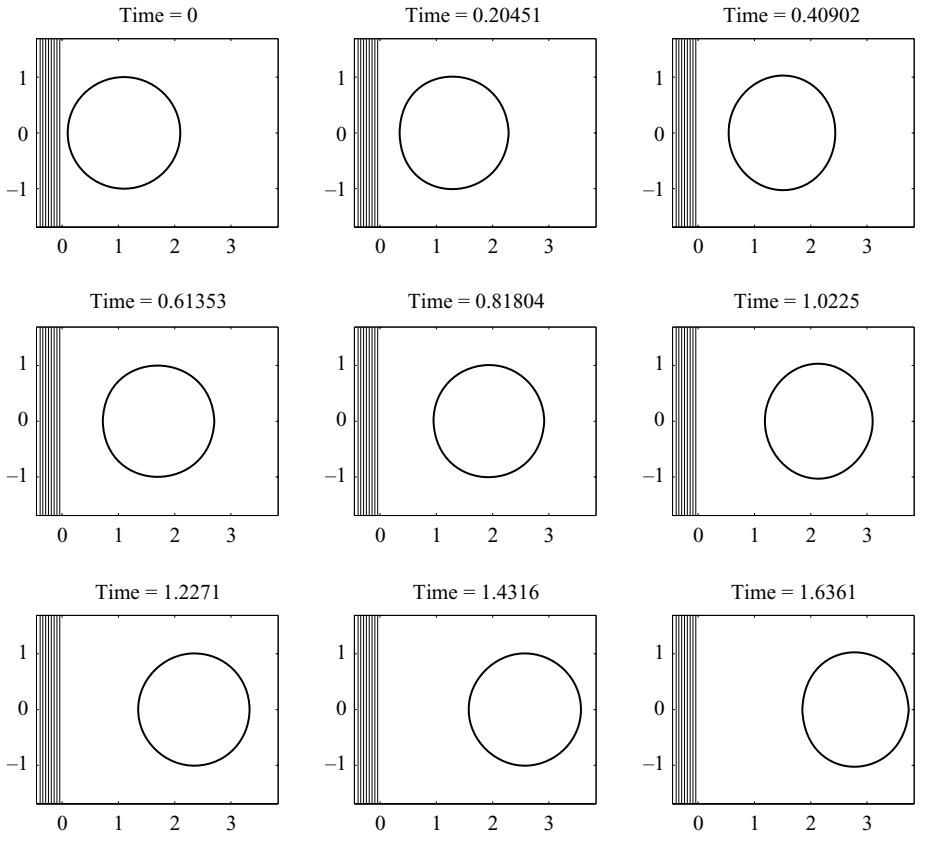

FIGURE 14. Bubble shape at equidistant time instants for $We = 0.12$. The wall is indicated by a set of straight parallel lines. Times are in units of $R_{t=0}/U_0$, distances in units of $R_{t=0}$.

2002). Figure 17 shows an increase of α with increasing distance to the wall that therefore can only be caused by deformation. Values of ψ_{11} are in the range 4–4.5, and those of ψ_{33} in the range 0.2–0.25, as in § 3.5.3. The importance of off-diagonal terms in the matrix $\boldsymbol{A}$ is similar to that in § 3.5.3.

It will now be shown that velocity U decreases with increasing deformation mainly due to the increased value of the well-known mass coefficient α. To explain the influence of deformation on translation, the Euler–Lagrange equation corresponding to generalized coordinate z, that is, the second row-equation of (2.19), is examined. It can be written in the following form:

$$\frac{1}{\mathscr{V}}\frac{\mathrm{d}}{\mathrm{d}t}\{2U\alpha\mathscr{V}\} - 2U^2\frac{\partial\alpha}{\partial z} + \frac{1}{\mathscr{V}}\frac{\mathrm{d}}{\mathrm{d}t}\left\{\mathscr{V}\sum_m^\infty \dot{b}_m\gamma_m\right\} + -2U\sum_m^\infty \dot{b}_m\frac{\partial\gamma_m}{\partial z} - 2\sum_{ij}\dot{b}_i\,\dot{b}_j\frac{\partial\psi_{ij}}{\partial z} = 0. \quad (3.31)$$

The histories of the dominant terms of (3.31) are shown in figure 19. This figure shows that the terms with partial derivatives with respect to z in (3.31) are only contributing in the vicinity of the wall, that is, at distances $z/R_{t=0} < 3.5$. For U_0-induced deformation at $We = 1.2$, the last term on the left-hand side of (3.31) turns

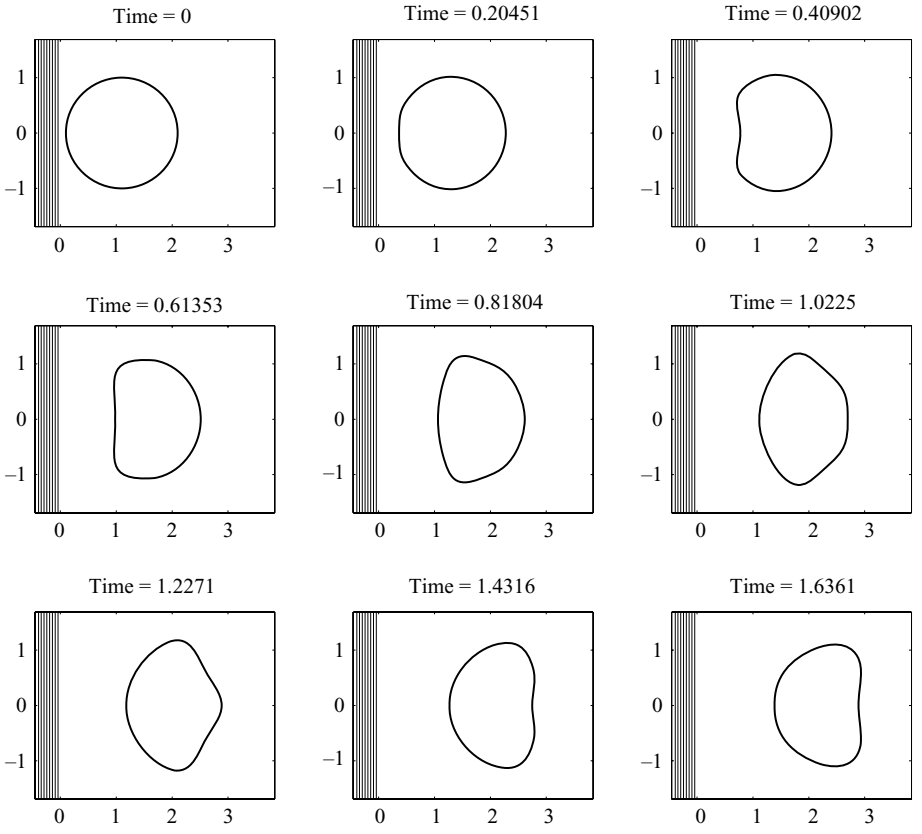

FIGURE 15. Bubble shape at equidistant time instants for $We = 1.2$. The wall is indicated by a set of straight parallel lines. Times are in units of $R_{t=0}/U_0$, distances in units of $R_{t=0}$.

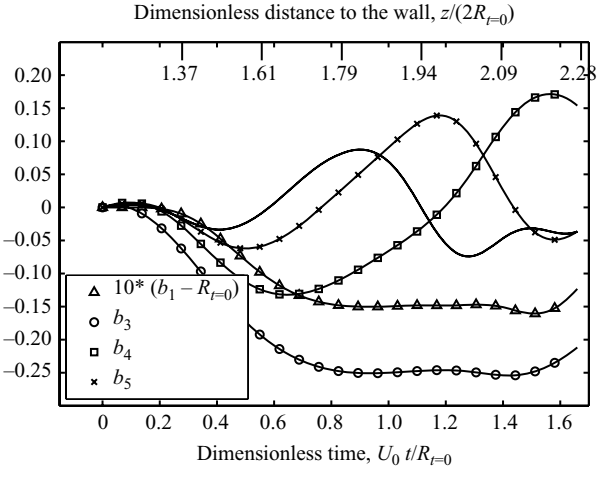

FIGURE 16. Histories of shape coefficients b_k ($k > 2$) and of $10(b_1 - 1)$ for an initially spherical bubble suddenly set into motion at $We = 1.2$. See figure 15 for the corresponding shape history. Also, the corresponding distances of the centroid to the wall, $z/2$, are shown on top. The plain solid line corresponds to b_6.

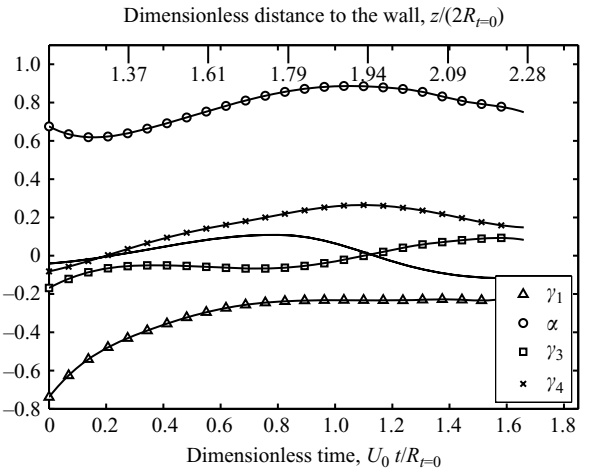

FIGURE 17. Histories of added mass coefficients α and γ_m for an initially spherical bubble suddenly set into motion at $We = 1.2$. See figure 15 for the corresponding shape history. Also, the corresponding distances of the centroid to the wall, $z/2$, are shown. The plain solid line corresponds to γ_5.

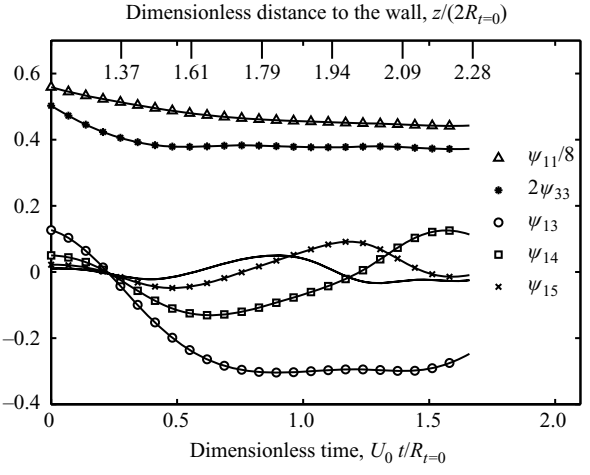

FIGURE 18. Histories of added mass coefficients ψ_{1j} ($j = 3, 4, 5$), $\psi_{11}/8$ and $2\psi_{33}$ for an initially spherical bubble suddenly set into motion at $We = 1.2$. See figure 15 for the corresponding shape history. The plain solid line corresponds to ψ_{16}.

out to be negligible, while for deformation-induced motion (§ 3.5) this term could not be neglected because the bubble could not get away from the wall.

Further away from the wall, velocity U is therefore given by (3.29) that in the present case can be written as

$$U \simeq (\alpha \not\curvearrowright U)|_{t=0} / (\alpha \not\curvearrowright) + \left\{ -\gamma_1 \dot{b}_1 - \sum_{j=3}^{\infty} \gamma_j \dot{b}_j \right\} \Big/ (2\alpha) \tag{3.32}$$

with the first term on the right-hand side comprising the value of $\alpha \not\curvearrowright U$ at time zero when all generalized velocities are zero except $U = U_0$. Because of the corresponding values of γ_m, the deformation velocities $\dot{b}_m$ corresponding to the lowest values of m yield the dominant deformation contributions in (3.32) at later times. The second

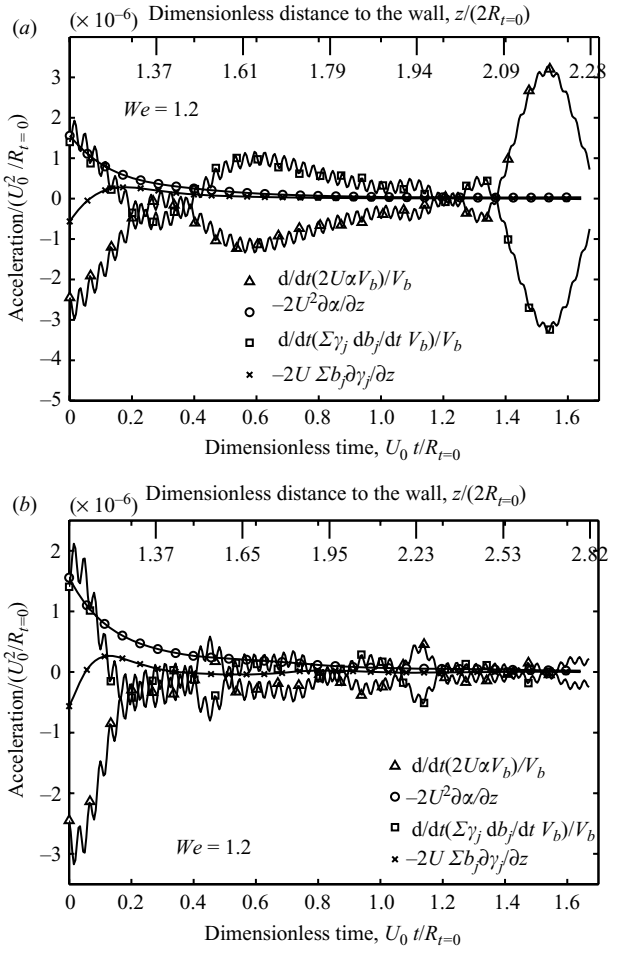

FIGURE 19. Histories of dimensionless accelerations for motion-induced bubble deformation at $We = 1.2$ (a) and $We = 0.12$ (b); $V_b = \forall$. The main contributions to the second Lagrange–Hamilton equation are shown. Note that the initial scaled accelerations are the same for both Weber numbers.

term on the right-hand side, $-\sum_m^\infty \dot{b}_m \gamma_m/(2\alpha)$ is at maximum 15 % of $U|_{t=0}$ for all strong deformations shown in figure 15, while U changes by more than 50 % at the same time. As a result, the velocity U is roughly inversely proportional to added mass α, with 30 % deviations due to the $\dot{b}_m\gamma_m$-terms of (3.32). There is a direct coupling between bubble shape and motion of the centroid (U) since the familiar added mass coefficient α depends on shape because α depends on the b_m-coefficients. This dependency on shape is dominant. However, some specific (per unit of mass) momentum of the motion of the centroid $\alpha \forall U$ is transformed to specific deformation momentum at the interface, the $\forall \dot{b}_m \gamma_m$ terms. For example, γ_1 is negative and asymptotically goes to a value of -0.2 with increasing distance to the wall (see figure 17), implying that isotropic expansion ($\dot{b}_1 > 0$) increases the momentum $2\alpha \forall U$ anywhere (see (3.32)). Expansion tends to propel the bubble centre away from the wall. The high-frequency oscillatory changes of b_1 (see (3.13) and § 3.5.5) therefore cause similar oscillatory changes in U. These high-frequency oscillations in U are in phase with the isotropic shape oscillations corresponding to b_1. As in the generic example

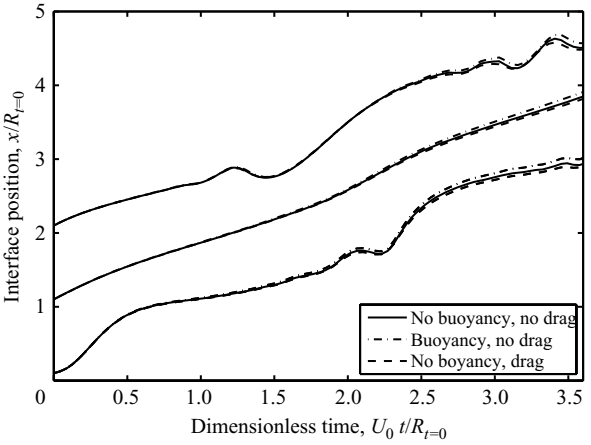

FIGURE 20. Comparison of the effects of gravity and Levich drag on long-term interfacial deformation for $We = \rho_L R_0 U_0^2/\sigma = 1.2$ and $p_\infty/(\rho_L U_0^2) = 8571$. The result with gravity and without drag is for $Bo = \tilde{g} R_0^2 \rho_L/\sigma = 0.01$ and the results for drag without gravity is for $Re = R_0 U_0 \rho_L/\mu = 926$. For a fluid with $\rho_L = 800$ kg m^{-3}, $\mu = 1.55 \cdot 10^{-4}$ kg.m s^{-1} and $\sigma = 0.07$ N m^{-1} and for $\tilde{g} = 9.8$ m s^{-12} these values correspond for example to a bubble with initial radius $R_0 = 0.328$ mm with initial velocity $U_0 = 0.545$ m s^{-1}. Positions of the leading edge, centroid and trailing edge are shown without the symbols of figure 13.

of § 3.5, these are the high frequencies that can also be observed in the accelerations, see figure 19. The apparent mirror symmetry for $z/R_{t=0} > 3.5$ in figure 19 of the two terms $\frac{\mathrm{d}}{\mathrm{d}t}\{2U\alpha\mathscr{V}\}/\mathscr{V}$ and $\frac{\mathrm{d}}{\mathrm{d}t}\{\mathscr{V}\sum_m^\infty \dot{b}_m\gamma_m\}/\mathscr{V}$ reflects the constancy of the left-hand side of (3.32). The remaining changes in each of the two terms on the left-hand side of (3.32) are mainly due to the non-isotropic deformation revealed by, for example, figure 15. For the term $\mathscr{V}\sum_m^\infty \dot{b}_m\gamma_m$ this is obvious (see also figures 16 and 17). For the term $2\alpha\mathscr{V}U$ this follows from the changes in α in figure 17. The added mass coefficient α increases with increasing degree of deformation (see above). The stronger the deformation, the slower the translational motion of the bubble. This trend was already concluded from figure 13, in the above, and is now explained.

3.6.3. *The effects of gravity and viscosity*

The results shown up to now have been obtained for Bond number equal to zero and Reynolds number infinitely large, that is, with the neglect of gravity and viscosity. To investigate the effect of gravity and viscosity, two test cases have been investigated with finite values of the Bond and the Reynolds numbers. In each of these test cases, three conditions have been prescribed: one without gravity and without drag, one with gravity and without drag, one without gravity and with drag. Two high Weber numbers (1.2 and 2.07) have been applied in order not to have more than one agency (surface tension) controlling the bubble shape. The total runtime has been made more than two times that of figure 13, while the same length scales as plotted in this figure have been employed. The results are shown in figure 20 and in figure 21. The corresponding dimensionless numbers are given in the captions, for figure 21 for example $We = \rho_L R_0 U_0^2/\sigma = 2.07$, $p_\infty/(\rho_L U_0^2) = 355$, $Bo = \tilde{g} R_0^2 \rho_L/\sigma = 0.0473$ or zero and $Re = R_0 U_0 \rho_L/\mu = 709$ or infinitely large. The results make clear why the runtime has been chosen so large: only at the latest times gravity and viscosity may introduce small deviations in shape. For a fluid with $\rho_L = 965$ kg m^{-3}, $\mu = 2.92 \cdot 10^{-4}$ kg.m s^{-1} and $\sigma = 0.05$ N m^{-1} and for $\tilde{g} = 9.8$ m s^{-2}

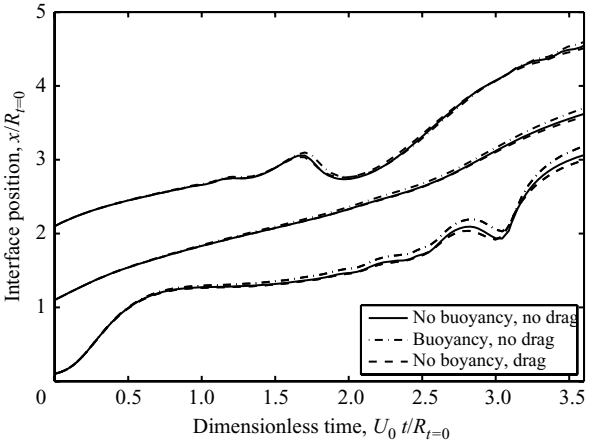

FIGURE 21. Comparison of the effects of gravity and Levich drag on long-term interfacial deformation for $We = \rho_L R_0 U_0^2/\sigma = 2.07$ and $p_\infty/(\rho_L U_0^2) = 355$. The result with gravity and without drag is for $Bo = \tilde{g} R_0^2 \rho_L/\sigma = 0.0473$ and the results for drag without gravity is for $Re = R_0 U_0 \rho_L/\mu = 709$. Positions of the leading edge, centroid and trailing edge are shown without the symbols of figure 13.

the dimensionless numbers of figure 21 correspond to a bubble with initial radius $R_0 = 0.463$ mm with initial velocity $U_0 = 0.463\,\mathrm{m\,s^{-1}}$, for example. Another example of practical fluid and flow conditions corresponding to the values of the dimensionless numbers chosen is given in the captions of figure 20.

The results show that if the Reynolds number exceeds 1000 and if the Bond number is less than 0.01 the effects of gravity and viscosity can be ignored at times less than $3R_0/U_0$, even if the Weber number is as large as 2.

4. Conclusions

The added mass tensor of a bubble moving and strongly deforming in incompressible fluid in the vicinity of a plane wall has been computed. The dynamics of axisymmetric bubble deformation at a distance from a plane solid wall have been computed with this added mass tensor, in which most coefficients relate to shape deformation. These dynamics have alternatively been computed with the BEM. No artificial viscosity was needed in the BEM to obtain stability. Full deformation computations can be accelerated by selecting an artificially low value of the polytropic constant C_p/C_v. Good agreement between results of the two methods has been found. Solutions of cases available in the literature are correctly reproduced. The explicit expressions for the added mass tensor could for isotropic (spherical) deformation be reduced to results known from a previous study. The coupled dynamics of motion and deformation is most conveniently described by a tensor with matrix $\boldsymbol{A}$. This symmetric matrix has relatively high values at the diagonal and the neighbouring off-diagonal places, as well as in the first row and column (corresponding to the fundamental radial oscillation mode and b_1). The coupling with the motion of the centroid is via the terms on the second row (and second column).

The Rayleigh–Plesset equation, governing isotropic deformation, has been extended with terms to account for arbitrary axisymmetric deformation and to account for the proximity of a plane wall. A governing equation for the important deformation mode connected to the second Legendre polynomial, P_2, has been presented and simplified

in order to obtain an equation for this mode that is similar to the Rayleigh–Plesset equation. The angular frequencies of periodic solutions of the linearized governing equations in the absence of a wall, like ω_{RP} for the isotropic mode, follow easily from the equations presented. Because of the presence of an U^2 term in the governing equation, motion of the bubble centre induces anisotropic deformation even at large distances from the wall. A periodically and anisotropically deforming bubble without initial velocity of the centroid is eventually always driven towards the wall because of the fact that shape deformation and oscillation couple to volume oscillations. The angular frequencies of periodic solutions are decreased if the distance to the wall is decreased. A strong coupling of anisotropic deformation modes with isotropic deformation exists. The frequency doubling of the relatively low frequencies of the anisotropic modes in the isotropic mode is explained. The frequency of this isotropic mode is even very close to the wall accurately given by

$$\omega_{RP}^2 \Big/ \left\{1 + R/z - \frac{3}{2}(R/z)^4 \Big/ (2\alpha)\right\}\Big|_{t=0}.$$

The resonance case introduced by Longuet-Higgins (1989*a*) is shown to have non-singular behaviour when ω_{RP} is equal to the twice the radian frequency of a fundamental deformation mode. The larger the amplitude of deformation components, the more the motion of the bubble centre is slowed down. It has been shown that the main reason for this is the increase of the 'classical' added mass coefficient α with increased deformation.

It has been shown in what cases, and how, the equation that dominates motion of the bubble centroid in many cases can be simplified. This simplified equation may facilitate prediction of motion of a deforming bubble in CFD programmes. When initially a bubble is set into motion away from a plane wall, the simplified equation of motion can further away from the wall be integrated, to yield the following equation for the velocity U of the centre:

$$U \simeq (\alpha U)|_{t=0}/(\alpha) + \left\{-\gamma_1 \dot{b}_1 - \sum_{j=3}^{\infty} \gamma_j \dot{b}_j\right\} \Big/ (2\alpha)$$

with the second term on the right-hand side about 15 % of the first term at maximum, even for cases of strong deformation. Since only the added mass coefficients γ_j need to be evaluated, the effect of strong deformation on motion of a bubble not too close to a plane wall is relatively easily computed with the above equation. This result holds when gravity and drag are negligible, but it has been shown that these agencies may be neglected in many practical cases of strong deformation. Criteria to specify the conditions of validity of the neglect of gravity and drag have been presented.

This work was financially supported by the EC-project AD-700-2.

REFERENCES

Abramowitz, M. & Stegun, I. A. 1972 *Handbook of Mathematical Functions*. Dover.

Auton, T. R., Hunt, J. C. R. & Prud'Homme, M. 1988 The force exerted on a body in inviscid, unsteady non-uniform rotational flow. *J. Fluid Mech.* **197**, 241–257.

Bagchi, P. & Balachandar, S. 2003 Inertial and viscous forces on a rigid sphere in straining flows at moderate Reynolds numbers. *J. Fluid Mech.* **481**, 105–148.

Benjamin, T. B. & Ellis, A. T. 1990 Self-propulsion of asymmetrically vibrating bubbles. *J. Fluid Mech.* **212**, 65–80.

Brennen, C. E. 1995 *Cavitation and Bubble Dynamics*. Oxford University Press.

Doinikov, A. A. 2004 Translational motion of a bubble undergoing shape oscillations. *J. Fluid Mech.* **501**, 1–24.

Eller, A. I. 1970 Damping constants of pulsating bubbles. *J. Acoust. Soc. Am.* **47**, 1469–1470.

Feng, Z. C. & Leal, L. G. 1995 Translational instability of a bubble undergoing shape oscillations. *Phys. Fluids* **7**, 1325–1336.

van der Geld, C. W. M. 2002 On the motion of a spherical bubble deforming near a plane wall. *J. Engng Math.* **42**, 91–118.

van der Geld, C. W. M. 2009 The dynamics of a boiling bubble before and after detachment. *Heat Mass Transfer* **45** (1), 831–846.

Gradsteyn, I. S. & Ryzhyk, I. M. 1980 *Table of Integrals, Series and Products*. Academic Press.

Hobson, E. W. 1955 *The Theory of Spherical and Ellipsoidal Harmonics*. Cambridge University Press.

Howe, M. S. 1995 On the force and moment of a body in an incompressible fluid, with application to rigid bodies and bubbles at low and high Reynolds numbers. *Q. J. Mech. Appl. Math* **48**, 401–426.

Kantorovich, L. V. & Krylov, V. L. 1958 *Approximate Methods of Higher Analysis*. Interscience.

Lamb, H. 1932 *Hydrodynamics*, 6th edn. Cambridge University Press.

Legendre, D., Borée, J. & Magnaudet, J. 1998 Thermal and dynamic evolution of a spherical bubble moving steadily in a superheated or subcooled liquid. *Phys. Fluids* **10** (6), 1256–1272.

Longuet-Higgins, M. S. 1989*a* Monopole emission of sound by asymmetric bubble oscillations. Part 1. Normal modes. *J. Fluid Mech.* **201**, 525–541.

Longuet-Higgins, M. S. 1989*b* Monopole emission of sound by asymmetric bubble oscillations. Part 2. An initial value problem. *J. Fluid Mech.* **201**, 543–565.

Longuet-Higgins, M. S. 1989*c* Some integral theorems relating to the oscillations of bubbles. *J. Fluid Mech.* **204**, 159–166.

Magnaudet, J. & Eames, I. 2000 The motion of high-Reynolds-number bubbles in inhomogeneous flows. *Annu. Rev. Fluid Mech.* **32**, 659–708.

Mei, C. C. & Zhou, X. 1991 Parametric resonance of a spherical bubble. *J. Fluid Mech.* **229**, 29–50.

Meiron, D. I. 1989 On the stability of gas bubbles rising in an inviscid fluid. *J. Fluid Mech.* **198**, 101–114.

Mougin, G. & Magnaudet, J. 2002 The generalized kirchhoff equations and their application to the interaction between a rigid body and an arbitrary time-dependent viscous flow. *Intl J. Multiph. Flow* **28**, 1837–1851.

Pelekasis, N. A. & Tsamopoulos, J. A. 1993 Bjerknes forces between two bubbles. Part 1. Response to a step change in pressure. *J. Fluid Mech.* **254**, 467–499.

Pozrikidis, C. 1997 *Introduction to Theoretical and Computational Fluid Mechanics*. Oxford University Press.

Prosperetti, A. 1977 Thermal effects and damping mechanisms in the forced radial oscillations of gas bubbles in fluids. *J. Acoust. Soc. Am.* **61**, 17–27.

Prosperetti, A. 1984 Bubble phenomena in sound fields: part two. *Ultrasonics* **22**, 115–123.

Telles, J. C. F. 1987 A self-adaptive coordinate transformation for efficient numerical evaluation of general boundary element integrals. *Intl J. Numer. Meth. Engng* **24**, 959–973.

Toose, E. M., van den Ende, H. T. M., Geurts, B. J., Kuerten, J. G. M. & Zandbergen, P. J. 1996 Axisymmetric non-Newtonian drops treated with a boundary integral method. *J. Engng Math.* **30**, 131–150.

Tsamopoulos, J. A. & Brown, R. A. 1983 Nonlinear oscillations of inviscid drops and bubbles. *J. Fluid Mech.* **127**, 519–537.

Versluis, M., Schmitz, B., von der Heydt, A. & Lohse, D. 2000 How snapping shrimp snap: through cavitating bubbles. *Science* **289**, 2114–2117.